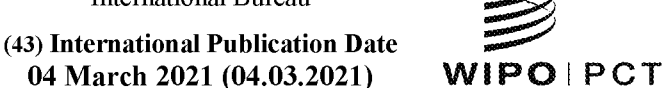
#### (12) INTERNATIONAL APPLICATION PUBLISHED UNDER THE PATENT COOPERATION TREATY (PCT)

(19) World Intellectual Property Organization

International Bureau





(10) International Publication Number WO 2021/036793 A1

(51) International Patent Classification:

A61K 45/00 (2006.01)

A61P 35/00 (2006.01)

how

(21) International Application Number:

PCT/CN2020/108776

(22) International Filing Date:

13 August 2020 (13.08.2020)

(25) Filing Language:

English

(26) Publication Language:

English

(30) Priority Data:

PCT/CN2019/102224

23 August 2019 (23.08.2019) CN

- (71) Applicants: NATIONAL INSTITUTE OF BIOLOGI-CAL SCIENCES, BEIJING [CN/CN]; 7 Science Park Rd., ZGC Life Science Park, Changping District, Beijing 102206 (CN). PEKING UNIVERSITY [CN/CN]; No. 5 Yiheyuan Rd., Haidian District, Beijing 100871 (CN).
- (72) Inventors: SHAO, Feng, 7 Science Park Rd., ZGC Life Science Park, Changping District, Beijing 102206 (CN). LIU, Zhibo; 7 Science Park Rd., ZGC Life Science Park, Changping District, Beijing 102206 (CN). WANG, Qinyang; 7 Science Park Rd., ZGC Life Science Park, Changping District, Beijing 102206 (CN). WANG, Yupeng; 7 Science Park Rd., ZGC Life Science Park, Changping District, Beijing 102206 (CN).
- (74) Agent: PANAWELL & PARTNERS, LLC; 1002-1005, China Life Tower, 16 Chao Yang Men Wai Street, Chaoyang District, Beijing 100020 (CN).
- (81) Designated States (unless otherwise indicated, for every kind of national protection available): AE, AG, AL, AM, AO, AT, AU, AZ, BA, BB, BG, BH, BN, BR, BW, BY, BZ, CA, CH, CL, CN, CO, CR, CU, CZ, DE, DJ, DK, DM, DO, DZ, EC, EE, EG, ES, FI, GB, GD, GE, GH, GM, GT, HN, HR, HU, ID, IL, IN, IR, IS, IT, JO, JP, KE, KG, KH, KN, KP, KR, KW, KZ, LA, LC, LK, LR, LS, LU, LY, MA, MD, ME, MG, MK, MN, MW, MX, MY, MZ, NA, NG, NI, NO, NZ, OM, PA, PE, PG, PH, PL, PT, QA, RO, RS, RU, RW, SA, SC, SD, SE, SG, SK, SL, ST, SV, SY, TH, TJ, TM, TN, TR, TT, TZ, UA, UG, US, UZ, VC, VN, WS, ZA, ZM, ZW.
- (84) Designated States (unless otherwise indicated, for every kind of regional protection available): ARIPO (BW, GH, GM, KE, LR, LS, MW, MZ, NA, RW, SD, SL, ST, SZ, TZ, UG, ZM, ZW), Eurasian (AM, AZ, BY, KG, KZ, RU, TJ, TM), European (AL, AT, BE, BG, CH, CY, CZ, DE, DK, EE, ES, FI, FR, GB, GR, HR, HU, IE, IS, IT, LT, LU, LV, MC, MK, MT, NL, NO, PL, PT, RO, RS, SE, SI, SK, SM, TR), OAPI (BF, BJ, CF, CG, CI, CM, GA, GN, GQ, GW, KM, ML, MR, NE, SN, TD, TG).

#### Published:

— with international search report (Art. 21(3))



(54) Title: PYROPTOSIS-INDUCED IMMUNOTHERAPY

(57) **Abstract:** Pyroptosis-induced immunotherapy is effected by activating a pore-forming, pyroptogenic molecule, wherein the activating induces tumor cell pryoptosis and causes tumor regression by T-cell mediated anti-tumor immunity.

#### Pyroptosis-Induced Immunotherapy

Inventors: Feng Shao, Zhibo Liu, Qinyang Wang, Yupeng Wang, all of Beijing, CN

Applicants: National Institute of Biological Sciences, Beijing

Peking University, Beijing, China

## [001] Introduction

**[002]** Bioorthogonal chemistry capable of operating in the living system is desirable for dissecting complex biological processes such as cell death and immunity<sup>1,2</sup>. Recent studies in innate immunity identify a gasdermin family of pore-forming proteins that executes inflammasome-dependent or -independent pyroptosis<sup>3-9</sup>. Pyroptosis is proinflammatory but its exact immunologic effect in disease contexts, particularly cancer immunity, is unclear.

## [003] Summary of the Invention

We disclose and exemplify a bioorthogonal chemical system (e.g., a cell-enterable [004] cancer-imaging probe Phe-BF<sub>3</sub> specifically desilylates and "cleaves" a silyl ether-containing carbamate linker). When the linker was attached to gold nanoparticle (NP) vehicle, the system achieved tumor-selective targeting for controlled release of a client GFP protein from the endocytosed NPs. Application of the system to a gasdermin triggered "clean" pyroptosis at the death execution step. Tumor cell pyroptosis induced by Phe-BF<sub>3</sub>-released gasdermin causes nearly complete regression of tumorgrafts including the 4T1 mammary carcinoma. This effect requires pore-forming activity of the gasdermin and occurs with both intravenous and intratumoral injection of Phe-BF3 and the NP-gasdermin conjugate. Pyroptosis-induced tumor regression is blocked in immune-deficient nude mice or upon T-cell depletion, and correlates with increased tumor-infiltrating lymphocytes. An ineffective injection regimen of one-round Phe-BF<sub>3</sub>+NP-gasdermin injection prominently sensitizes the 4T1 tumors to anti-PD1 therapy, demonstrating synergy. Thus, our desilylation-based bioorthogonal system is a powerful chemical biology tool, including its application to pyroptosis-induced inflammation to trigger effective antitumor immunity or improve the efficacy of checkpoint blockade immunotherapy. The invention provides method and compositions for treating cancer by activating a poreforming, pyrpotogenic molecule (e.g. a gasdermin), wherein the activating induces tumor cell pryoptosis and causes tumor regression by T-cell mediated anti-tumor immunity. Moreover, activation transforms the tumor from immunologically cold to hot, and synergizes with anti-PD1 therapy.

**[006]** In an aspect the invention provides a method of inducing an antitumor immune response in a person in need thereof, comprising: (a) administering to the person a pyroptosis activator; and (b) detecting a resultant pyroptosis-induced antitumor immune response.

- [007] In embodiments of any aspect of the invention:
- [008] the method comprises: administering to the person an anti-PD1 therapeutic wherein the pyroptosis activator and the anti-PD1 therapeutic synergistically induce tumor regression in the person; and detecting a resultant tumor regression in the person;
- [009] the pryoptosis activator is a gasdermin agonist;
- [010] the pyroptosis activator is a bioothogonal agent that releases an activationally restrained gasdermin in tumor cells of the person;
- [011] the pyroptosis activator is a bioothogonal agent that releases an activationally restrained gasdermin in tumor cells of the person, wherein the gasdermin is conjugated to a matrix (such as a nanoparticle) in the cells, and the biothorganal agent releases (deconjugates) the gasdermin from the matrix;
- [012] the gasdermin is activationally restrained though a silyl ether linkage, and the agent is an organotrifluoroborate that cleaves the linkage and thereby releases the gasdermin from activational restraint;
- [013] the linker comprises an ortho-carbamoylmethylene silyl-phenolic ether, in which the carbamate carbon is linked to the gasdermin;
- [014] the ortho-carbamoylmethylene silyl-phenolic ether comprises a silyl ether moiety selected from: trimethylsilyl ether (TMS), triethylsilyl ether (TES), tert-butyldimethylsilyl ether (TBS/TBDMS), tert-butyldiphenylsilyl ether (TBDPS), and triisopropylsilyl ether (TIPS);
- [015] the organotrifluoroborate comprises a boroamino acid (BAA), e.g. PheBF3; and/or
- [016] the activationally restrained gasdermin is conjugated to a nanoparticle (NP).
- [017] In an aspect the invention provides a method for releasing in a cell a client molecule from a silyl ether containing linker, comprising: introducing into the cell an organotrifluoroborate under conditions wherein the organotrifluoroborate reacts with the silyl ether to desilylate and release from the linker the client molecule; and optionally detecting resultant release of the client molecule.
- [018] In embodiments of any aspect of the invention:
- [019] the linker comprises an ortho-carbamoylmethylene silyl-phenolic ether, in which the carbamate carbon is linked to the client molecule;
- [020] the linker comprises a silyl ether that is trimethylsilyl ether (TMS), triethylsilyl ether (TES), tert-butyldimethylsilyl ether (TBS/TBDMS), tert-butyldiphenylsilyl ether (TBDPS), or triisopropylsilyl ether (TIPS);
- [021] the linker is joined to a nanoparticle;

- [022] the organotrifluoroborate comprises a boroamino acid (BAA), e.g. PheBF3;
- [023] the client molecule is a label (e.g. GFP), a cytotoxic drug (e.g. imatinib, pemetrexed), or a tumor suppressor protein (e.g. gasdermin);
- [024] the cell is a cancer cell;
- [025] the linker is joined to a nanoparticle, the client molecule is a gasdermin, the cell is a cancer cell of a tumor, and the method activates the gasdermin in the cell to stimulate pyroptosis in the cell and achieve anti-tumor immunotherapy;
- [026] the introducing step comprises administering the organotrifluoroborate to a person in need of anti-tumor immunotherapy, and optionally detecting a resultant pyroptosis-induced antitumor immune response; and/or
- [027] the method further comprises administering to the person an anti-PD1 therapeutic wherein the organotrifluoroborate and the anti-PD1 therapeutic synergistically induce tumor regression in the person; and optionally, detecting a resultant tumor regression in the person.
- [028] In an aspect the invention provides compositions, reagents and kits formulated and adapted specifically for the subject methods.
- [029] The invention encompasses all combinations of the particular embodiments recited herein.
- [030] Brief Description of the Drawings
- [031] Figs. 1a-g. A desilylation-based orthogonal chemistry by which Phe-BF $_3$  efficiently releases a client molecule from a silyl ether-containing carbamate linker.
- [032] **a**, Schematic representation of Phe-BF<sub>3</sub>-mediated desilylation that can release the fluorescence-"caged" coumarin from a designed silyl ether-containing carbamate linker. **b-d**, Fluorescence-"decaging" and liquid-chromatography assays of Phe-BF<sub>3</sub>-mediated desilylation of TESO-Coumarin (TESO-C), TBSO-Coumarin (TBSO-C) or TIPSO-Coumarin (TIPSO-C). **b**, **c**, Photographs (**b**) and quantification (**c**) of coumarin fluorescence are shown. **d**, Blue and magenta mark the maximum absorbance wavelength of TESO/TBSO-Coumarin (350 nm) and free coumarin (435 nm), respectively. **e**, Summary of the reaction efficiency for Phe-BF<sub>3</sub> or sodium fluoride (NaF)-catalyzed desilylation towards TESO/TBSO/TIPSO-Coumarin. **f**, Fluorescence-emission assay of possible desilylation of TESO-Coumarin (10  $\mu$ M) by various biologically relevant nucleophilic anions (5 mM for GSH, 20 mM for H<sub>2</sub>O<sub>2</sub>, and 10 mM for others). The coumarin fluorescence intensity spectra were acquired at 37°C in PBS with  $\lambda_{ex}$  = 370 nm and  $\lambda_{em}$  = 435 nm. **g**, Summary of desilylation efficiency of TESO-Coumarin (10  $\mu$ M) by FDA-approved organofluorines. **e**, **g**, Reaction efficiency was determined by HPLC; ND, not detected. Data in **b-e**, **g**, are representative of at least three independent experiments.

## [033] Figs. 2a-h. Phe-BF<sub>3</sub>-mediated desilylation can release GFP from the silyl ether carbamate-linked NP\_GFP *in vitro* and selectively in tumors in mice.

a, Design of Phe-BF<sub>3</sub>-mediated desilylation of the silyl ether carbamate-linked NP\_GFP for releasing GFP from the NP. Fluorescence of GFP is quenched when it is conjugated to the NP; desilylation-induced "cleavage" of the linker causes release of free GFP. b, In vitro assay of desilylation-induced release of GFP from the NP\_GFP conjugates by Phe-BF<sub>3</sub>, NaF or another indicated organofluorine. The reactions were centrifugated to precipitate the NP and obtain the supernatant, as illustrated in Fig. 7a. T, the total reaction; S, the supernatant; P, the NP pellet. The asterisk indicates the loading control reaction prior to centrifugation. c, d, Assays of Phe-BF<sub>3</sub> desilylation-induced release of GFP from the NP GFP conjugates in mammalian cells. HeLa, EMT6, 4T1, or priBMDM (primary bone marrow-derived macrophage) cells were first treated with NP\_GFP (1 mg/mL) for 12 h and then for another 24 h with Phe-BF<sub>3</sub> (100 μM) or NaF as a control. c, Cell lysates were centrifuged and subjected to anti-GFP and anti-GAPDH immunoblotting analyses. d, Representative confocal fluorescence images of the treated priBMDM cells (scale bar, 20 µm). e, Representative PET-CT 3D projection images of tumorbearing mice intravenously injected with [89Zr]GFP, [89Zr]NP GFP or [18F]Phe-BF<sub>3</sub>, t, tumor; l, liver; k, kidney; gb, gallbladder.  $\mathbf{f}$ , Assay of Phe-BF<sub>3</sub> desilylation-induced release of mNeonGreen-NLS from the NP mNeonGreen-NLS conjugates in tumor-bearing mice. Representative confocal fluorescence images of tumor sections. Scale bar, 20 µm (left) and 5 µm (right). g, h, Numbers (g) and percentages (h) of mNeonGreen-NLS-positive cells in the examined tumor sections (N=2 for the NP\_mNeonGreen-NLS only group and =4 for the NP\_mNeonGreen-NLS+Phe-BF<sub>3</sub> treated group; two-tailed unpaired Student's t-test, \*\*\*\*P < 0.0001). e-g, BALB/c mice implanted subcutaneously with the 4T1 cancer cells were used. Data are representative of two  $(\mathbf{d}, \mathbf{f}, \mathbf{g}, \mathbf{h})$  or three  $(\mathbf{b}, \mathbf{c})$  independent experiments.

# [035] Figs. 3a-d. Phe-BF<sub>3</sub>-mediated desilylation can release gasdermin from NP\_GA3 to trigger pyroptotic cell death.

[036] **a**, Design of Phe-BF<sub>3</sub>-mediated desilylation of the silyl ether carbamate-linked NP\_GA3 for releasing the gasdermin from the NP and inducing pyroptosis. Purified gasdermin-N and -C noncovalent complex (N+C) was conjugated to the NP to generate NP\_GA3. **b-d**, Pyroptosis assay of cultured mammalian cells treated with the NP\_GA3 conjugates and Phe-BF<sub>3</sub>. HeLa, EMT6, 4T1, or priBMDM cells were treated as indicated. NP+GA3 means the unconjugated GSDMA3 protein (N+C) mixed with the NP. GA3<sup>Mut</sup>, the pore-forming activity-deficient E14K/L184D mutant version of GSDMA3 (N+C). **b**, Phase-contrast images of HeLa (Left) and EMT6 (Right) cells (arrows, cells with pyroptotic morphology). **c**, Flow cytometry plots of

propidium iodide (PI) and Annexin V-fluorescein isothiocyanate (FITC)-stained cells. **d**, Percentages of PI/Annexin V-positive pyroptotic cells measured by the flow cytometry analyses. Data are shown as mean  $\pm$  s.d. from three biological replicates; two-tailed unpaired Student's *t*-test was performed (\*\*\*P < 0.001, \*\*\*\*P < 0.0001). All data are representative of three independent experiments.

- [037] Figs. 4a-h. Tumor cell pyroptosis induced by NP\_GA3+Phe-BF<sub>3</sub> treatment triggers tumor regression in mice.
- **[038] a**, Representative PET-CT 3D projection images of 4T1 tumor-bearing mice intravenously injected with [89Zr]GA3, [89Zr]NP\_GA3 or [18F]Phe-BF3. *t*, tumor; *l*, liver; *k*, kidney; *gb*, gallbladder. **b-h**, Assays of tumor growth in mice treated with NP\_GA3+Phe-BF3. **b**, NP\_GA3+Phe-BF3 treatment scheme in BALB/c mice implanted subcutaneously with the 4T1 (7 mice per group) (**c-f**) or EMT6 (6-8 mice per group) (**g**, **h**). **c-h**, The tumor-bearing mice were intravenously injected (i.v.) or intratumorally injected (i.t.) with NP\_GA3 or Phe-BF3 alone or in combination. GA3<sup>Mut</sup>, the pore-forming activity-deficient E14K/L184D mutant version of GSDMA3 (N+C). **c**, **g**, Tumor volume of individual mouse at indicated time points after implantation. **d**, **h**, Average tumor volumes of each group of mice (*P* values are included in Fig. 9c for **d**). **e**, **f**, Photograph (**e**) and weight (**f**) of the 4T1 tumors on day 26 after inoculation. **d**, **f**, **h**, Data (mean ± s.e.m.) are shown and two-tailed unpaired Student's *t*-test was performed (\* *P* < 0.05, \*\* *P* < 0.01, \*\*\* *P* < 0.001, \*\*\*\* *P* < 0.0001). Data are representative of three (**c-f**) or two (**g**, **h**) independent experiments.
- [039] Figs. 5a-j. NP\_GA3+Phe-BF<sub>3</sub>-induced pyroptosis triggers effective antitumor immunity and can synergize with anti-PD1 checkpoint blockade therapy.
- **1040 a**, PI staining assay of NP\_GA3+Phe-BF<sub>3</sub>-induced tumor cell pyroptosis in mice. The 4T1 tumor-bearing BALB/c mice were treated with PBS (n=3), NP\_GA3+Phe-BF<sub>3</sub> (n=4) or NP\_GA3<sup>Mut</sup>+Phe-BF<sub>3</sub> (n=4) similarly as in Fig. 4b. Prior to assay, PI was intravenously injected into the mice and shown are representative images of the tumor sections (scale bar, 100 μm). **b**, Assays of tumor growth in Nu/Nu mice treated with NP\_GA3+Phe-BF<sub>3</sub> (6-8 mice per group). The treatment scheme is the same as depicted in Fig. 4b. **c**, Numbers of tumor-infiltrating lymphocytes (TILs) per gram of 4T1 tumors and percentages of Treg cells. Data were acquired from 6 (the PBS and NP\_GA3+Phe-BF<sub>3</sub> groups) or 7 (the NP\_GA3<sup>Mut</sup>+Phe-BF<sub>3</sub> group) mice from three independent experiments. **d**, Effect of antibody depletion of T cells on NP\_GA3+Phe-BF<sub>3</sub>-induced tumor regression. Anti-CD4 (n=9) or CD8 (n=7) or an isotype control antibody (n=9) were intraperitoneally injected into the 4T1 tumor-bearing mice prior to NP\_GA3+Phe-BF<sub>3</sub> treatment. The 4T1 tumor-bearing mice were also treat

a control (n=8). **e**, **f**, scRNA-Seq analyses of the effect of NP\_GA3+Phe-BF<sub>3</sub> treatment on tumor immune microenvironment. **e**, *t*-Distributed stochastic neighbor embedding (*t*-SNE) plot of 18,069 RNA-sequenced single CD45<sup>+</sup> immune cells from PBS (n=2) and NP\_GA3+Phe-BF<sub>3</sub> (n=2)-treated 4T1 tumors. **f**, *t*-SNE density plots of random simple sampling 7,000 CD45<sup>+</sup> immune cells from each group. **g-j**, Assay of the synergistic effect between NP\_GA3+Phe-BF<sub>3</sub> treatment and anti-PD1 blockage therapy on tumor growth. 4T1 tumor-bearing mice were treated with PBS (n=7), anti-PD1 (n=8) or NP\_GA3+Phe-BF<sub>3</sub> (n=7) alone or in combination (n=8). **g**, 4T1 tumor growth curve. **h**, **i**, Photograph (**h**) and weight (**i**) of 4T1 tumors at the end of indicated treatments. **j**, Scheme for the combined treatment. **b-d**, **g**, **i**, Data (mean  $\pm$  s.e.m.) were analyzed by two-tailed unpaired Student's *t* test (\* P < 0.05, \*\* P < 0.01, \*\*\*\* P < 0.001, NS, not significant). Data shown are representative of two (**a**, **b**, **d-i**) independent experiments.

- [041] Figs. 6a-d. Phe-BF<sub>3</sub>-mediated desilylation of a designed silyl ether-containing carbamate linker and synthetic routes of related compounds. a, Chemical structures of silylphenolic ether-conjugated coumarin derivatives. b, Proposed mechanism for Phe-BF<sub>3</sub> catalyzing desilylation of the silyl ether that triggers decarboxylation on the carbamate and therefore release of the coumarin. c, Synthetic route of TESO-Coumarin. TBSO-Coumarin (TBSO-C) and TIPSO-Coumarin (TIPSO-C) were synthesized via a similar strategy. d, Synthetic route of the silyl ether-containing carbamate linker used to conjugate the NP.
- **[042]** Figs. 7a-d. Assay of Phe-BF<sub>3</sub> desilylation-induced release of GFP from NP\_GFP and biodistribution of [<sup>89</sup>Zr]GFP and [<sup>89</sup>Zr]NP\_GFP in mice. **a**, Workflow of assaying Phe-BF<sub>3</sub> desilylation-induced release of GFP from NP\_GFP *in vitro*. The samples were subjected to immunoblotting and Coomassie blue staining analysis in Fig. 2b. **b**, Expression of LAT1 transporter in the four cells assayed in Fig. 2c. **c**, Representative dynamic PET-CT 3D projection images of 4T1 tumor-bearing mice at 1, 6, 12, 18 h after intravenous injection of [<sup>89</sup>Zr]GFP or [<sup>89</sup>Zr]NP\_GFP. *t*, tumor; *l*, liver. **d**, Representative confocal fluorescence images of HeLa cells transfected with a plasmid expressing mNeonGreen-NLS (scale bar, 20 μm). The nuclear localization sequence (NLS) is derived from the SV40 protein. Data (**b**, **d**) are representative of two independent experiments.
- [043] Figs. 8a-c. Phe-BF<sub>3</sub>-mediated desilylation can release gasdermin from NP\_GA3 to trigger cell death. a, b, Preparation of the gasdermin-N and -C noncovalent complex of GSDMA3 protein (GA3-(N+C)) used for conjugation onto the NP. Engineered GSDMA protein containing a PreScisson protease (PPase) cleavage site between the gasdermin-N and -C domain was recombinantly purified and cleaved *in vitro* to obtain the GA3-(N+C) protein. a, Coomassie

blue staining of the prepared GSDMA3 proteins. **b**, ATP-based viability analysis of mouse CT26 cells electroporated with the prepared GSDMA3 protein. **c**, ATP-based viability analysis of HeLa, EMT6 and 4T1 cells treated with NP\_GA3 or Phe-BF<sub>3</sub> alone or in combination. GA3<sup>Mut</sup>, the pore-forming activity-deficient E14K/L184D mutant version of GSDMA3 (N+C). **b**, **c**, Data are shown as mean  $\pm$  s.d.; two-tailed unpaired Student's *t*-test was performed (\*\*\*\**P* < 0.0001). All data are representative of at least three independent experiments.

- [044] Figs. 9a-e. Biodistribution of [89Zr]GA3 and [89Zr]NP\_GA3 and evaluation of the side effect of NP\_GA3+Phe-BF<sub>3</sub> treatment in mice. a, b, Dynamic PET-CT 3D projection images of 4T1 tumor-bearing mice at 2, 6, 12, 18 h after the intravenous injection of [89Zr]GA3 or [89Zr]NP\_GA3. t, tumor; l, liver. c, P values for tumor regression data in Fig. 4d (two-tailed unpaired Student's t-test). d, Records of mouse body weight after indicated treatments (8 or 9 mice per group) (data are shown as mean ± s.d.). e, Representative histological H&E staining of liver and kidney tissues from mice intravenously injected with PBS, NP\_GA3, Phe-BF<sub>3</sub>, NP\_GA3+Phe-BF<sub>3</sub> or NP\_GA3<sup>Mut</sup>+Phe-BF<sub>3</sub>. Data shown are representative of three (d) or two (e) independent experiments.
- [045] Figs 10a-g. Tumor cell pyroptosis induced by NP\_GA3+Phe-BF<sub>3</sub> treatment increases the tumor-infiltrating lymphocytes. a, PI staining assay of NP\_GA3+Phe-BF<sub>3</sub>-induced tumor cell pyroptosis in mice (an independent experiment from that in Fig. 5a) (scale bar, 100 μm). b, e, f, Gating strategy (b) and representative flow cytometry plots for assessing 4T1 tumor-infiltrating CD3<sup>+</sup>T cells (e) or Foxp3<sup>+</sup>CD4<sup>+</sup> regulatory T cells (f) following indicated treatments. c, d, Immunofluorescence staining of CD3<sup>+</sup>T cells within the 4T1 tumors.

  Representative fluorescence images of CD3-PE stained-4T1 tumors following treatment with PBS (n=4), NP\_GA3+Phe-BF<sub>3</sub> (n=4) or NP\_GA3<sup>Mut</sup>+Phe-BF<sub>3</sub> (n=6). Scale bar, 200 μm (c), 50 μm (Left in d) and 20 μm (Right in d). f, g, Flow cytometry analysis of CD4<sup>+</sup> or CD8<sup>+</sup> T cells depletion by the corresponding antibody. Data shown are representative of two (a, c, d) or three (e, f) independent experiments.
- **[046]** Figs. 11a-d. Tumor-infiltrating immune cells subtypes analysis by single-cell RNA-sequencing (scRNA-Seq). a, Gating strategy and representative flow cytometry plots for the enrichment of 4T1 tumor-infiltrating single CD45<sup>+</sup> immune cells. b, Heatmap of ten immune cell clusters with unique signature genes. Colors on top of the map indicate different immune cell clusters. Three or four selective marker genes are listed alongside. c, *t*-SNE plot of 18,069 RNA-sequenced 4T1 tumor-infiltrating single CD45<sup>+</sup> immune cells. d, Expression patterns of signature genes of the corresponding cell clusters on the *t*-SNE plot. All data shown are representative of two independent experiments.

[047] Figs. 12a-c. scRNA-Seq analyses indicate that T lymphocytes are attracted and activated in NP\_GA3+Phe-BF<sub>3</sub>-treated 4T1 tumors. a, t-SNE plots of tumor-infiltrating single CD45<sup>+</sup> immune cells of PBS-treated (n=2, 10,171 cells) and NP\_GA3+Phe-BF<sub>3</sub>-treated (n=2, 7,898 cells) 4T1 tumors (Left) and the relative frequencies of different clusters (Right). b, c, Expression levels of protumoral and immunosuppressive gens (b) and proinflammatory chemokine, T/NK cell activation or effector genes (b) in immune cells. Paired quantile-quantile (Q-Q) plots were used to compare the gene expression levels of CD45<sup>+</sup> immune cells between PBS and NP\_GA3+Phe-BF<sub>3</sub>-treated 4T1 tumors. *P* values were calculated using Wilcoxon rank-sum test. All data shown are representative of two independent experiments.

#### [048] Description of Particular Embodiments of the Invention

[049] The following descriptions of particular embodiments and examples are provided by way of illustration and not by way of limitation. Those skilled in the art will recognize a variety of noncritical parameters that can be changed or modified to yield essentially similar results. All publications, patents, and patent applications cited herein, including citations therein, are hereby incorporated by reference in their entirety for all purposes. Unless contraindicated or noted otherwise, in these descriptions and throughout this application, the terms "a" and "an" mean one or more, the term "or" means and/or.

We sought to determine whether a PET-imaging small molecule can be based to develop a bioorthogonal reaction that can function in the in vivo system. Previously, we designed an organotrifluoroborate-based "kit-like" <sup>18</sup>F-radiolabeling scheme <sup>18,35,36</sup>. Using this method, we prepared a class of amino acid mimetics, boramino acids (BAAs) that can be used as cancer imaging probes (because their amino acid transporters are often highly expressed in cancer)<sup>37</sup>. Phenylalanine trifluoroborate (Phe-BF<sub>3</sub>) is a representative BAA with a highly similar structure to phenylalanine (Phe) except for the replacement of carboxylate (-COO) with trifluoroborate (-BF<sub>3</sub>). Compared with <sup>18</sup>F-fluorodeoxylglucose (FDG), the standard PET imaging agent for clinical cancer diagnosis, Phe-BF3 exhibits a comparable sensitivity but a higher specificity in labeling tumors in mice<sup>37</sup>. BAAs also show non-specific uptake in the bone, which is thought to be caused by defluorination of the trifluoroborate group <sup>38-40</sup>. Free fluoride can catalyze a rapid and efficient desilylation reaction and is commonly used to remove the protecting silyl ether group in organic synthesis 41,42. We wondered whether Phe-BF3 could also catalyze efficient desilylation and if so whether the reaction could be developed into a useful bioorthogonal system, therefore making Phe-BF<sub>3</sub> a perturbing probe for tumor-selective protein activation<sup>37</sup>. To pursue this idea, we employed an *ortho*-carbamovlmethylene silyl-phenolic

ether system, in which the carbamate carbon is linked to a client molecule coumarin (Fig. 1a and Fig. 6a). Desilylation of this system will trigger elimination of the carbamate, leading to breakdown of the amide bond<sup>43,44</sup> (Fig. 6b) and therefore release of the coumarin. Free coumarin, as opposed to the amine-blocked coumarin in the silyl-phenolic ether system, is highly fluorescent, thus providing a simple and quantitative assay for Phe-BF<sub>3</sub>-mediated desilylation. We also introduced a para-N,N-dimethylaminoacetamide group into the design to gain water solubility as well as for future conjugation to a carrier molecule or a matrix (Fig. 1a and Fig. 6b). To optimize the desilylation efficiency, the silyl group was diversified into triethylsilyl (TES), tert-butyldimethyl silyl (TBS), or triisopropyl silyl (TIPS) (Fig. 1a and Fig. 6a); the corresponding three compounds, referred to as TESO-, TBSO- and TIPSO-Coumarin, respectively, were synthesized (Fig. 6c). Following 4-h incubation with Phe-BF<sub>3</sub>, TESO-Coumarin, but not TIPSO-Coumarin, released free coumarin extensively as a result of the desilylation reaction while TBSO-Coumarin only reacted weakly (Fig. 1b, c). Liquid chromatography-mass spectrometry (LC-MS) revealed that 98% of TESO-Coumarin and less than 20% of TBSO-Coumarin were desilylated by Phe-BF<sub>3</sub> while TIPSO-Coumarin remained untouched (Fig. 1d, e). As expected, incubation with sodium fluoride led to complete desilylation of TESO-Coumarin and TBSO-Coumarin but had no effect on TIPSO-Coumarin. The decreasing reactivity observed with TESO-, TBSO- and TIPSO-Coumarin suggests a steric hindrance on the silica atom for Phe-BF<sub>3</sub>-mediated desilylation, echoing the situation of sodium fluoride-induced desilylation<sup>45</sup>.

[051] We noticed that Phe-BF<sub>3</sub>-mediated desilylation of TESO- or TBSO-Coumarin could be completed instantly when the concentrations of both reactants were increased from 100 μM to 10 mM. Such an extraordinarily fast reaction is counterintuitive to the presumed, free fluoride intermediate-mediated catalysis because defluorination of Phe-BF<sub>3</sub> is a first-order reaction featuring a slow kinetics (it takes about 10,000 minutes to release 50% of fluoride from trifluoroborate<sup>46</sup>). Indeed, we were not able to detect free fluoride during the rapid desilylation of coumarin conjugates by NMR analyses. Thus, Phe-BF<sub>3</sub>-mediated desilylation can also proceed through an alternative mechanism that involves no free fluoride intermediate. Supporting this notion, organic chemists have used tetrabutylammonium difluorotriphenylsilicate, instead of free fluoride, to remove silyl ether<sup>47</sup>, in which the fluoride is transferred directly from the difluorotriphenylsilicate to the empty *d*-orbital of the silica atom on the silyl ether<sup>48</sup>.

[052] TESO-Coumarin (as well as the other two silyl ether-linked compounds) are highly stable and showed no spontaneous desilylation even after 12-h incubation in phosphate-buffered

saline (PBS) (Fig. 6e). Further, treating TESO-Coumarin with cellular concentrations of H<sub>2</sub>O<sub>2</sub>, GSH or other biologically relevant anions, including Cl<sup>-</sup>, Γ, and NO<sub>3</sub><sup>-</sup>, caused no release of free coumarin (Fig. 1f). The specificity of silyl ether to Phe-BF<sub>3</sub> agrees with the fact that the Si-O bond has much lower energy (368 kJ/mol) than the Si-F bond (565 kJ/mol), but higher than the bonds between Si and other atoms, which also explains why silyl ether can be selectively removed by fluoride in organic synthesis. Considering over 10% of FDA-approved drugs contain fluorine<sup>49</sup>, we assayed several fluorine-derived drugs including leflunomide, 5-fluorouracil (5-FU), capecitabine and FDG, and found that none of them, under the same condition used for Phe-BF<sub>3</sub>, were capable of releasing coumarin from TESO-Coumarin (Fig. 1g). Taken together, the intrinsic stability of the TES silyl ether linkage and its robust/specific cleavage by Phe-BF<sub>3</sub> indicate practical utility to be used for controlled release of bioactive molecules in the living system.

[053] Gold nanoparticle (NP) is a biocompatible delivery vehicle and has been approved by the FDA for clinical trials in humans<sup>50</sup>. NP has also been widely used in biological applications including drug delivery and bio-imaging<sup>51,52</sup>. NP has a selectivity for tumors owing to the enhanced permeability and retention (EPR) effect towards the tumor lesion as well as its superior internalization by cancer cells<sup>53,54</sup>. To further exploit Phe-BF<sub>3</sub>-mediated desilylation, we anchored the TES silyl-phenolic ether to NPs. Specifically, NPs were decorated with MeO-PEG-thiol (for better solubility and biocompatibility) mixed with 5% dibenzyl cyclooctyne (DBCO)-PEG-thiol. The TES silyl-phenolic ether was then conjugated to the decorated NPs through a copper-free "click" reaction between the DBCO and an azide added to the paradimethylaminoacetamide group (Fig. 6d). In addition, we replaced the coumarin with green fluorescence protein (GFP) via a thiol-maleimide linkage between the carbamate and Cys-147 in GFP (mutated from Ser-147), generating the TES silyl ether-containing NP\_GFP material (Fig. 2a). In this design, Phe-BF<sub>3</sub>-mediated desilylation shall trigger the same chemical reaction as that in TESO-Coumarin, resulting in liberation of the GFP from the NPs (Fig. 2a). To test this idea, purified NP\_GFP materials were treated with Phe-BF<sub>3</sub>, or sodium fluoride as a positive control, or another fluorine-containing compound in vitro for 4 h, and the reactions were centrifuged to precipitate the NPs (Fig. 7a). Nearly all GFP molecules were found to be released into the supernatants by Phe-BF<sub>3</sub> or sodium fluoride treatment (Fig. 2b). In contrast, incubation of NP\_GFP in PBS alone did not result in appearance of GFP in the supernatants. Echoing the situation in TESO-Coumarin, treatment with leflunomide, 5-FU, capecitabine or FDG also caused no release of GFP from NP\_GFP (Fig. 2b). Thus, Phe-BF<sub>3</sub>-mediated desilylation of the TES silvl ether is also highly effective in releasing a protein client.

NPs can efficiently enter mammalian cells through the endocytic pathway<sup>55</sup>. This allowed us to test whether Phe-BF<sub>3</sub>-mediated desilylation can really function inside living cells. For this, primary mouse bone marrow-derived macrophages (priBMDMs), human cervical carcinoma cell line HeLa, and murine mammary carcinoma EMT6 and 4T1 cells were treated with NP GFP (1 mg/mL) and then stimulated with 100 μM Phe-BF<sub>3</sub> or sodium fluoride. All these four cells expressed the LAT1 transporter that could uptake extracellular Phe-BF<sub>3</sub> (Fig. 7b). Immunoblotting showed that Phe-BF<sub>3</sub> treatment could effectively deconjugate NP\_GFP, evident from appearance of free GFP in the supernatants of centrifuged lysates (Fig. 2c). The deconjugation should occur on the endocytosed NP GFP as sodium fluoride that could not enter the cells caused no release of GFP (Fig. 2c). Importantly, the specific responses to Phe-BF<sub>3</sub> occurred in all the four diverse types of mammalian cells, indicating a generality of our method. NPs exhibit strong absorption of light between 200 nm to 600 nm, causing fluorescence quenching of the GFP immobilized on the NPs<sup>56</sup>; thus, cells treated with NP\_GFP alone showed no green fluorescence. However, upon stimulation with Phe-BF<sub>3</sub>, strong GFP fluorescence was detected, particularly in the primary BMDMs (Fig. 2d). This indicates that the desilylationreleased GFP remains functional in live mammalian cells.

Phe-BF<sub>3</sub>-treated cells maintained normal morphology with intact nuclei and membrane integrity (Fig. 2d). In fact, trifluoroborate-derived imaging probes have already been systematically evaluated in many cancer cells and animal models with no negative effects on cell proliferation and animal viability observed 18,57. We have also demonstrated that Phe-BF<sub>3</sub>, even when used at the high 25-mM concentration, exhibits little cytotoxicity<sup>37</sup>. This encouraged us to investigate the feasibility of using Phe-BF<sub>3</sub> to achieve controlled protein activation in the tumor in mice. When tail-vein injected into mice that had been subcutaneously engrafted with the 4T1 mouse mammary carcinoma cells, [18F]Phe-BF<sub>3</sub> was found to accumulate in the tumor within 1 h (Fig. 2e), owing to the high expression of the cognate LAT1 transporter in cancer cells. The remainder of injected [18F]Phe-BF<sub>3</sub> was rapidly cleared via the kidney; the gallbladder (gb) also contained a certain level of [18F]Phe-BF<sub>3</sub> as a result of hepatobiliary excretion (Fig. 2e). We also examined the distribution of intravenously injected NP\_GFP in the tumor-bearing mice by PET imaging. For this, Zirconium-89 (89Zr) was prepared through a Y(p, n)Zr reaction in a 14.6-MeV cyclotron, and the purified isotope (final specific activity > 1 Ci/µmol) was used to label the GFP protein as previously described<sup>58</sup>. When injected into mice, nearly all free [89Zr]GFP went to the liver within 1 h, with little penetration to the tumor lesion due to its poor circulation in the blood (Fig. 7c). In contrast, NP\_[89Zr]GFP was found to accumulate in the tumor at 6 h post-injection. NP\_[89Zr]GFP also appeared in the liver as expected, but this should

not be a concern because liver uptake of Phe-BF<sub>3</sub> was almost negligible<sup>37</sup> (Fig. 2e). Thus, the distribution of NP\_GFP and Phe-BF<sub>3</sub> overlaps only in the tumor, indicating that the orthogonal desilylation reaction can achieve tumor-selective targeting *in vivo*. Dynamic PET imaging scan further revealed that NP\_GFP had the highest enrichment in the tumor but the lowest level in the liver at 18 h after injection (Fig. 7c), indicating that this time point should be the optimal one for administration of Phe-BF<sub>3</sub>.

[056] We then tested whether Phe-BF<sub>3</sub> could catalyze the desired desilylation and liberate the client protein from the NP conjugates in the tumor-bearing mice. To increase the detection sensitivity, we replaced the GFP with a much brighter fluorescent protein mNeonGreen<sup>59</sup> and also incorporated a SV40-derived nuclear-localization sequence (NLS) at the carboxyl terminus of mNeonGreen. In this design, nuclear targeting of the released mNeonGreen will concentrate the fluorescence signal and aid the detection of Phe-BF<sub>3</sub>-mediated desilylation in the tissue. As expected, free mNeonGreen-NLS showed exclusive nuclear localization when expressed in HeLa cells (Fig. 7d). In mice injected with NP\_ mNeonGreen-NLS alone, no green fluorescence was detected in the tumor sections (Fig. 2f, g), agreeing with the high stability of the TES silyl ether linkage. Notably, additional injection of Phe-BF<sub>3</sub> into the mice caused evident appearance of nucleus-localized mNeonGreen in the tumor samples (Fig. 2f, g). Statistical data suggested that about 15% of cells in the tumor were positive for the mNeonGreen signal (Fig. 2h). These analyses provide a definitive proof that Phe-BF<sub>3</sub>-mediated desilylation of the TES silyl ether is applicable for tumor-selective activation or release of a protein molecule.

[057] As introduced earlier, the gasdermin-N domain, when unleashed from the C-terminal inhibitor gasdermin-C domain, translocates to the plasma membrane and oligomerizes there to form pores, thus executing pyroptotic cell death. The gasdermin-N domain could be an ideal application target of the Phe-BF<sub>3</sub>-mediated desilylation system for two reasons. First, the gasdermin-N domain, when immobilized onto the large-size NPs, is "caged" and completely inactive; it will perforate the plasma membrane only upon being released from the NPs by Phe-BF<sub>3</sub>-mediated desilylation (Fig. 3a). Second, pyroptosis is known to be highly proinflammatory, but its effect on the tumor has not been investigated due to the lack of approaches capable of inducing tumor cell pyroptosis without affecting other signaling pathways. To test this idea, we chose GSDMA3, a potent gasdermin whose inactive monomer as well as oligomeric pore are both structurally characterized<sup>6,31</sup>. For technical consideration, we mutated both cysteine residues in the gasdermin-C domain of GSDMA3 so that conjugation to NPs would only take place via the cysteine residues in the gasdermin-N domain. Recombinant GSDMA3 as well as its gasdermin-N and -C noncovalent complex (N+C) was purified to homogeneity (Fig. 8a). This

cysteine-mutant version of the noncovalent complex behaved similarly as the corresponding cysteine-intact complex<sup>6</sup> and induced extensive pyroptosis when electroporated into CT26 cells (Fig. 8b). The GSDMA3 noncovalent complex was then conjugated to the 60-nm NPs through the TES silyl-ether linker similarly as that to obtain NP\_GFP, generating the NP\_GA3 material (Fig. 3a). The NP\_GA3 was then used to treat mouse BMDMs, HeLa, EMT6 or 4T1 cells with for 24 h, and the cells were subjected to second treatment with Phe-BF<sub>3</sub>. Importantly, cells with evident pyroptotic morphology, characterized by swelling and bubbling, were observed following treatments with both agents (Fig. 3b). Administration of Phe-BF<sub>3</sub> or NP\_GA3 alone, or unconjugated GA3 and NP, did not cause cell pyroptosis. Previous studies show that the GSDMA3 E14K/L184D mutant is devoid of the pore-forming activity and therefore cannot execute pyroptosis<sup>6,31</sup>. We found that the same point mutation (GA3<sup>Mut</sup>) also diminished the pyroptosis-inducing activity of NP\_GA3 (Fig. 3b).

[058] Pyroptotic cells are positive for both Annexin-V and propidium iodide (PI) staining, which can be quantified by flow cytometry. Using this assay, we found that NP\_GA3+Phe-BF<sub>3</sub> treatment rendered ~ 40%, 35%, and 20% of HeLa, EMT6, and 4T1 cells, respectively, to undergo pyroptosis (Fig. 3c, d). The percentage of pyroptosis in primary BMDMs was even higher (about 80%) due to its strong phagocytic capacity (Fig. 3c, d). Again, cells treated with NP\_GA3<sup>Mut</sup>+Phe-BF<sub>3</sub> showed no differences in Annexin-V and PI staining from the control cells or cells treated with a single agent (Fig. 3c, d), indicating that the observed pyroptosis owes to the pore-forming activity of GSDMA3 released from the NPs by Phe-BF<sub>3</sub>-mediated desilylation. It is worth mentioning that NP itself is known to weakly inhibit cell proliferation. We did observe a subtle cell viability decrease with NP\_GA3 (Fig. 8c). However, the effect occurred independently of the pore-forming activity of NP\_GA3 and did not require Phe-BF<sub>3</sub>, and therefore does not affect our analyses of the effect of pyroptosis on the tumor.

[059] When injected to the 4T1 tumor-bearing mice, unconjugated [89Zr]GA3, like GFP, was rapidly and predominantly trapped in the liver with little uptake in the tumor even at 18 h after injection (Fig. 9a). NP\_[89Zr]GA3 showed a better biocompatibility, most of which could stay in the blood for 2 h after injection. Like NP\_GFP, NP\_GA3 also showed apparent tumor targeting at 12 h after infection and then started to be cleared through the hepatobiliary system (Fig. 9b). At 18 h post injection, the tumor uptake of NP\_[89Zr]GA3 reached a plateau with the maximal level up to 15 %ID/g.

[060] Given that the distribution of NP\_GA3 and Phe-BF<sub>3</sub> also converged only in the tumor tissue (Fig. 4a), we examined whether Phe-BF<sub>3</sub> desilylation-induced GSDMA3 activation (i.e., pyroptosis) could promote tumor clearance in mice. BALB/c mice engrafted subcutaneously

with the 4T1 cancer cells were injected intravenously with NP GA3 (5 mg/kg) at day 6 followed by two sequential intravenous injections of Phe-BF<sub>3</sub> (50 mg/kg) at day 7 and 8, respectively (Fig. 4b). The treatment cycle was repeated twice at day 9 and 12 to augment the extent of pyroptosis induction. In PBS-treated control mice, the volume of the 4T1 tumors increased expectedly by about 20-fold in 2 weeks (Fig. 4c-e). Strikingly, upon treatments with NP\_GA3+Phe-BF<sub>3</sub>, most of the tumors became reddish in the first few days, and afterwards strong necrosis inside the tumors and massive tumor shrinkage were observed (Fig. 4c-e and Fig. 9c). A pronounced growth delay of about 15 days was seen with NP\_GA3+Phe-BF<sub>3</sub>-treated mice, compared with the control mice; at day 25, minimal and negligible tumor burden could be observed (Fig. 4c-e). In contrast, mice treated for three cycles with NP GA3 or Phe-BF3 alone behaved similarly as the PBS-treated mice and showed normal and aggressive tumor growth (Fig. 4b-d and Fig. 9c). This indicates that the observed tumor shrinkage results from Phe-BF<sub>3</sub>mediated desilylation and release of GSDMA3 from the NPs. Furthermore, when the poreforming activity-deficient NP\_GA3<sup>Mut</sup> proteins were used in combination with Phe-BF<sub>3</sub>, there was no tumor shrinkage and the treated mice showed aggressive tumor growth as the PBStreated mice (Fig. 4c-e and Fig. 9c). Measuring the tumor weight confirmed the antitumor effect caused by the pyroptotic activity of GSDMA3 released from the NPs (Fig. 4f). A similar tumor regression effect was observed with NP GA3+Phe-BF<sub>3</sub> treatment in mice engrafted with another mouse tumor cell line EMT6, which was also dependent upon the pyroptosis-inducing activity of GSDMA3 (Fig. 4g, h). This indicates that the antitumor effect of Phe-BF<sub>3</sub> desilylationinduced GSDMA3 activation is not limited to a particular tumor model. While NP\_GA3+Phe-BF<sub>3</sub> treatment induced strong tumor regression, the treated mice showed no notable weight loss and abnormalities in major organs such as the liver and the kidney (Fig. 9d, e). These indicate that Phe-BF<sub>3</sub> desilylation-triggered release and activation of GSDMA3 is well tolerated in mice, highlighting a biological safety of this type of new therapeutic strategy.

[061] In addition to intravenous injection, we also performed intratumoral injection of NP\_GA3+Phe-BF<sub>3</sub> and observed the same regression of the implanted 4T1 tumors in mice (Fig. 4c-f). This indicates that the therapeutic effect seen with intravenous injection is likely due to GSDMA3 activation at the tumor local site, which agrees with the observation that targeting of NP\_GA3 and Phe-BF<sub>3</sub> converges on the tumor tissue in mice. Furthermore, we tail-vein injected PI into mice that had been subjected to three cycles of sequential NP\_GA3 and Phe-BF<sub>3</sub> treatments and then examined the tumor slice for possible pyroptotic cells. In this assay, quite a number of PI-positive necrotic cells appeared in tumors derived from NP\_GA3+Phe-BF<sub>3</sub>-treated mice (Fig. 5a and Fig. 10a). As tumor progression is always associated with hypoxia and

nutrient deprivation, there were also PI-positive cells in tumors from PBS or NP\_GA3<sup>Mut</sup>-treated mice, but the number was apparently much lower than that in tumors from NP\_GA3+Phe-BF<sub>3</sub>-treated mice (Fig. 5a and Fig. 10a). This data demonstrates pyroptotic cell death in the mouse tumor grafts, which is caused by Phe-BF<sub>3</sub> desilylation of the silyl ether in NP\_GA3.

In the *in vivo* PI staining assay, we also noticed that the PI-positive cells were relatively a small fraction of the entire cell population in the implanted 4T1 tumor. Such low percentage is not unexpected given that Phe-BF<sub>3</sub>-induced deconjugation of NP\_GA3 only caused about 20% pyroptosis in cultured 4T1 cells (Fig. 3, d). However, the low ratio of tumor cell pyroptosis could not directly account for the drastic regression observed with the entire tumor (Fig. 4c-f). Considering the proinflammatory nature of pyroptosis, we wondered whether the tumor regression involves functioning of the immune system. To this end, we turned to the athymic nude (Nu/Nu) mice which lack mature T cells. This type of immune-deficient mice could support the growth of implanted 4T1 tumors similarly as the wild-type BALB/c mice (Fig. 5b). However, the same scheme of NP\_GA3+Phe-BF<sub>3</sub> treatment did not cause any tumor regression in the Nu/Nu mice (Fig. 5b). This finding indicates a requirement of T cells for GSDMA3 activation-induced tumor clearance. Consistently, flow cytometry revealed a drastically increased CD3<sup>+</sup> T cell population in tumors from NP\_GA3+Phe-BF<sub>3</sub>-treated mice, compared with tumors from PBS-treated mice (Fig. 5c and Fig. 10b). Anti-CD3 fluorescent imaging of the tumor tissue confirmed the massive T cell infiltration (Fig. 10c, d). Among the T cells, both the CD4<sup>+</sup> and the CD8<sup>+</sup> subpopulations were elevated while the percentage of CD4<sup>+</sup>Foxp3<sup>+</sup> T regulatory (Treg) cells, the negative regulator of antitumor immunity, were decreased in tumors from NP\_GA3+Phe-BF<sub>3</sub>-treated mice (Fig. 5c and Fig. 10b, e, f). Importantly, injection with the pyroptosis-deficient NP\_GA3<sup>Mut</sup> (plus Phe-BF<sub>3</sub>), which could not cause tumor regression, also did not induce T cell infiltration into the tumors (Fig. 5c and Fig. 10c, e, f). To validate and investigate the role of T cells in pyroptosis-induced antitumor immunity, we then depleted CD4<sup>+</sup> or CD8<sup>+</sup> T cells in 4T1 tumor-bearing mice by the anti-CD4 or anti-CD8 antibody, respectively, which was confirmed by flow cytometry of the splenocytes (Fig. 10g). Notably, depletion of either CD4<sup>+</sup> or CD8<sup>+</sup> T cells blocked NP\_GA3+Phe-BF<sub>3</sub>-induced tumor regression while the isotype control antibody showed no such effect (Fig. 5d and Fig. 10g). This indicates that not only the cytotoxic T cells but also the CD4<sup>+</sup> T helper cells are critical for pyroptosis-induced tumor regression. Agreeing with this finding, cancer immunology studies in the past 10 years have also recorded an important role of CD4<sup>+</sup> T cells for full activation of CD8+ T cells in cancer immunotherapy<sup>60,61</sup>, including in mouse 4T1 tumor model<sup>62</sup>.

[063] To obtain a full picture of pyroptosis-induced immunological changes in the tumor

microenvironment (TME), the CD45<sup>+</sup> leukocytes from 4T1 tumors of PBS-treated as well as NP-GA3+Phe-BF<sub>3</sub>-treated mice were subjected to single-cell RNA sequencing (scRNA-Seq) analyses (Fig. 11a). A total of 18,069 single immune cells from two control mice (10,171 cells) and two therapeutic mice (7,879 cells) were sequenced, which were clustered into 10 subsets on the two-dimensional t-SNE map (Fig. 5e). These subsets were identified and classified by the high and differential expression of genes marking classical immune cell populations (Fig. 11bd). Analyses of the scRNA-Seq data indicated that NP-GA3+Phe-BF3-treated tumors, compared with PBS-treated tumors, had increased populations of CD4<sup>+</sup>, CD8<sup>+</sup> and NK (natural killer) cells but decreased percentages of monocytes, neutrophils and myeloid-derived suppressor cells (MDSCs) (Fig. 5f and Fig. 12a). The macrophage population also increased in the therapeutic group, which was due to the M1 subpopulation because the percentage of cells expressing the M2 marker (Arg1) was instead decreased (Fig. 5f and Fig. 12b). Further analyses of the expression data revealed that genes encoding the chemotactic cytokines such as Ccl5, Cxcl9 and Cxcl10 as well as genes important for T and/or NK cell activation (Cd69 and Klrk1) had elevated expression in NP-GA3+Phe-BF<sub>3</sub>-treated tumors (Fig. 12c). In addition, expression of effector genes critical for antitumor immunity (like Ifng, Gzms and Fasl) were also upregulated in the therapeutic tumor samples. In contrast, genes that are known to be protumoral or immunosuppressive, such as Csf1, Vegfa, Arg1, Cd274 (encode PD1) and Pdcd1lg2 (encode PD-L2), showed decreased expression upon NP-GA3+Phe-BF<sub>3</sub> treatment (Fig. 12b). These analyses provide a global view of pyroptosis-induced immunological changes within the TME, which well agrees and collaborates the potent antitumor effect observed in NP-GA3+Phe-BF<sub>3</sub>treated mice.

[064] Immune checkpoint blockade therapy, such as anti-PD1/PD-L1 and anti-CTLA4, has been highly successful in clinical treatment of a broad range of cancers. However, this emerging promising cancer therapy suffers from the low response rate, limiting its application to a wide population of cancer patients<sup>63,64</sup>. The exact reason for the general resistance of cancer patients to checkpoint blockade therapy is still unclear and probably varies among different cancers<sup>65</sup>. One widely accepted view is that inflammation within the TME is low or ineffective for inducing sufficient infiltration and/or activation of the lymphocytes, and for this reason the checkpoint blockade-resistant tumors are considered to be "cold"<sup>66,67</sup>. We wondered whether pyroptosis-induced inflammation within the TME could "heat" some "cold" tumors and therefore synergize with the checkpoint blockade agent in mounting robust antitumor immunity. To test this idea, we chose the 4T1 tumor model, which is known to be "cold" and did not respond to (intraperitoneal) anti-PD1 antibody treatment (Fig. 5g-i). We reduced the three

rounds of NP-GA3+Phe-BF<sub>3</sub> treatments to one round, which became insufficient to prevent tumor growth and cause any regression effect (Fig. 5g-i). However, when one round of NP-GA3+Phe-BF<sub>3</sub> treatment was followed by anti-PD1 antibody treatments (Fig. 5j), a strong synergistic effect was observed, evident from the drastic shrinkage of the tumor volume and the markedly reduced tumor weight (Fig. 5g-i). This result confirms our finding that induction of tumor cell pyroptosis can trigger robust T cell-mediated anticancer immunity and can synergize with the checkpoint blockage therapy.

[065] In these examples we first designed an organotrifluoroborate-meditated desilylation reaction that functions both in the cell culture system and in the animal system. Specifically, a silyl ether-containing carbamate linker is desilylated by a cell-enterable small molecule Phe-BF<sub>3</sub>, leading to "cleavage" of the linker. This bioorthogonal chemistry, when combined with NP-mediated delivery, shows a high tumor selectivity and can readily release any bioactive macromolecule from the NP, as we have demonstrated with GFP and gasdermin. Conceivably, Phe-BF<sub>3</sub>-mediated desilylation, which is biocompatible and highly efficient, can be adapted to other settings or combined with other chemical methods for establishing new chemical biology systems. As a fluorine-containing amino acid mimetic, [<sup>18</sup>F]Phe-BF<sub>3</sub> is an established PET imaging probe. Our study shows that a biocompatible small molecule such as Phe-BF<sub>3</sub> can possess dual functions of probing and perturbing a biological system.

[066] We further applied Phe-BF<sub>3</sub>-mediated desilylation chemistry to the gasdermin protein by "caging" its pore-forming activity to NPs through the silyl ether-containing carbamate linker. This application for the first time enabled us to directly stimulate pyroptotic cell death in the tumors in mice, which unexpectedly reveals a potent antitumor effect of pyroptosis. We further found that pyroptosis-induced tumor regression is mediated by T cells that show increased infiltration into the tumors. Pyroptosis or more specifically gasdermin activation in tumor cells not only initiates effective antitumor immunity on its own but also can synergize with the anti-PD1 checkpoint blockade therapy. This finding demonstrates that pyroptosis-induced inflammation within the TME can turn the "cold" tumor into the "hot" tumor, showing that a gasdermin agonist or a pyroptosis activator can be used to improve the efficacy of cancer immunotherapy.

**[067]** A role of necrotic or lytic cell death in promoting anticancer immune response was considered several decades ago owing to immune-dependent anticancer effect observed with certain cell-killing chemotherapeutic drugs<sup>68,69</sup>, for which the term "immunogenic cell death" is coined<sup>70,71</sup>. Recent studies show that cancer cell necroptosis, another form of programmed necrosis mediated by the death receptor complex-RIPK3-MLKL axis under the context of

caspase inhibition, can promote antitumor immunity  $^{72,73}$ . A very recent report also suggests that iron overload-induced ferroptosis in cancer cells is activated by IFN $\gamma$  released from antigen-primed CD8<sup>+</sup> T cells during cancer immunotherapy  $^{74}$ . It has been suggested for necroptosis that DAMPs-induced maturation of dendritic cells, cross-priming of CD8<sup>+</sup> T cells as well as IFN $\gamma$  production underlie its antitumor immunity  $^{72,73}$ , in which the cross-priming appears to rely on activation of the NF- $\kappa$ B proinflammatory signaling. It has also been noted that fibroblast necroptosis, initiated by the more upstream death-receptor ligand, instead suppresses NF- $\kappa$ B-mediated production of proinflammatory factors from the dying cells  $^{75}$  and is unable to stimulate co-cultured macrophages to produce proinflammatory cytokines  $^{76}$ . Different from these previous studies in which necroptosis is activated at the steps upstream in the cell death program, the Phe-BF3-mediated bioorthogonal desilylation reaction developed in our study allows us to kill cancer cell at the final executioner step in pyroptosis (i.e., pore formation by the unleashed gasdermin protein) without affecting other signaling events.

#### [068] Materials and Methods

## [069] Chemical reagents, plasmids and antibodies

[070] 5-Fluorouracil/5-FU (920052), Leflunomide (448506), Capecitabine (392078) and Fluoro-2-deoxy-D-glucose/FDG (D234500) were obtained from J&K Scientific. Synthesis and characterization of compounds-(1-6) are shown in Fig. 6c, 1d. Other chemical reagents and solvents used in this study were purchased from Sigma-Aldrich, J&K Scientific, Energy Chemical or Thermo Fisher Scientific. All NMR spectra were recorded at room temperature (RT) on a Bruker Avance 400 MHz or 600 MHz spectrometer. Signals are presented as ppm, and multiplicity identified as s = single, br = broad, d = doublet, t = triplet, q = quartet, m = multiplet; coupling constants are in Hz. Concentration of the compounds was performed by rotary evaporation without heating at an appropriate reduced pressure. Chemistry yields refer to the isolated pure chemicals.

[071] Complementary DNA (cDNA) for mouse *Gsdma3* was synthesized by our in-house gene synthesis facility. cDNAs for *eGFP* and *mNeonGreen* were gifts from Dr. P. Xu (Institute of Biophysics, Chinese Academy of Sciences). The cDNAs were cloned into a modified pET vector with an N-terminal 6×His-SUMO tag for recombinant expression in *E. coli.* cDNA for *mNeonGreen*-NLS was generated by standard PCR cloning strategy with a reverse primer containing the SV40 nuclear localization signal (NLS) sequence (5′-CCG AAA AAA CGT AAA GTT-3′). The cDNA was inserted into a modified pCS2-3×Flag vector for transient expression in HeLa cells. Primers used for generating point mutations were designed using an

online program (https://www.agilent.com/store/primerDesignProgram.jsp). All plasmids were verified by DNA sequencing.

[072] For FACS analyses of tumor-infiltrating lymphocytes, PE-conjugated anti-mouse CD3 (clone 17A2), FITC-conjugated anti-mouse CD4 (clone RM4.5), and APC-conjugated anti-mouse CD8 (clone 53-6.7) were purchased from BioLegend. eFluor 450-conjugated anti-mouse Foxp3 antibody (clone FJK-16s) was obtained from Invitrogen. The PD1 antibody used for treating 4T1 tumors was a gift from BeiGene. For immune cell depletion, anti-mouse CD4 (clone GK1.5) and isotype control (clone LTF-2) antibodies were produced by BioXcell, and anti-mouse CD8 was a gift from Dr. J. Sui (National Institute of Biological Sciences, Beijing). Anti-LAT1 antibody (D-10) was obtained from Santa Cruz Biotechnology. Anti-GFP (11814460001) and anti-GAPDH antibodies were obtained from Roche and Sigma-Aldrich, respectively.

#### [073] Synthesis and isolation of TESO-, TBSO- and TIPSO-Coumarin

The synthetic routes for TESO-, TBSO-, and TIPSO-Coumarin are essentially the same [074] and illustrated in Fig. 6c. Briefly, coumarin-NCO (500 mg, 2.48 mmol) was dissolved in dry THF (15 ml), and then mixed with Compound 5 (1.0 equiv., 2.37 mmol) and dibutyltin dilaurate (DBTL, 0.05 equiv., 0.12 mmol) under  $N_2$  atmosphere. The solution was stirred under refluxing THF for 24 h. Without washing, the organic layer was removed under reduced pressure. The residue was purified by flash chromatography to obtain silyl ether-conjugated coumarin as the white solid (40% yield). TESO-coumarin:  $^{1}$ H NMR (600 MHz, DMSO- $d_6$ )  $\delta$  7.75 – 7.65 (m, 2H), 7.62 - 7.51 (m, 2H), 7.44 (dt, J = 8.8, 2.6 Hz, 1H), 6.85 (dd, J = 8.5, 3.9 Hz, 1H), 6.24 (s, 1H), 5.14 (d, J = 15.1 Hz, 2H), 2.48 – 2.30 (m, 9H), 0.92 (dt, J = 25.9, 7.8 Hz, 9H), 0.75 (q, J = 25.9) 8.0 Hz, 3H). TBSO-coumarin:  ${}^{1}$ H NMR (400 MHz, DMSO- $d_6$ )  $\delta$  10.51 (s, 1H), 10.31 (s, 1H), 7.73 - 7.64 (m, 2H), 7.56 (d, J = 1.9 Hz, 2H), 7.43 (dd, J = 8.6, 1.9 Hz, 1H), 6.88 (d, J = 8.7 Hz, 1H), 6.24 (s, 1H), 5.13 (s, 2H), 3.74 (s, 2H), 3.35 (s, 6H), 2.38 (s, 3H), 0.95 (s, 9H), 0.23 (s, 6H). <sup>13</sup>C NMR (101 MHz, DMSO) δ 160.06, 153.83, 153.23, 153.22, 149.51, 142.79, 131.89, 126.32, 126.06, 121.74, 121.23, 118.67, 114.38, 114.30, 111.91, 104.46, 61.98, 45.26, 43.96, 25.53, 18.02, 17.88, 8.41, -4.44. TIPSO-coumarin: <sup>1</sup>H NMR (400 MHz, DMSO-d6) δ 10.28 (s, 1H), 7.70 (d, J = 8.7 Hz, 1H), 7.64 (d, J = 1.9 Hz, 1H), 7.57 - 7.49 (m, 2H), 7.43 (dd, J = 8.7, 1.8 Hz, 1H)1H), 6.86 (d, J = 8.8 Hz, 1H), 6.27 - 6.20 (m, 1H), 5.19 (s, 2H), 2.55 (s, 5H), 2.41 - 2.37 (m, 3H), 1.07 (d, J = 1.3 Hz, 16H), 1.04 (s, 3H). HPLC-MS was used to analyze stability of the synthesized TESO-, TBSO-, and TIPSO-Coumarin.

[075] Synthesis and isolation of the TESO-Linker for NP conjugation (Compound 7)

[076] Compound 6 (1.0 equiv., 1 mmol) and DBTL (0.05 equiv., 0.05 mmol) were dissolved in acetone (10 mL) under N<sub>2</sub> atmosphere. The solution was stirred under refluxing THF for 48 h. Without washing, the organic layer was removed under reduced pressure. The residue was purified by flash chromatography to obtain Compound 7. This synthetic route is shown in Fig. 6d.  $^{1}$ H NMR (400 MHz, Chloroform-d)  $\delta$  7.75 – 7.68 (m, 1H), 7.53 (dd, J = 5.6, 3.3 Hz, 2H), 7.35 (s, 1H), 6.74 (d, J = 8.6 Hz, 1H), 5.08 (s, 2H), 3.81 (d, J = 6.0 Hz, 2H), 3.57 (s, 2H), 3.46 – 3.38 (m, 3H), 3.21 (q, J = 4.8, 3.5 Hz, 2H), 2.67 (s, 6H), 1.71 (dd, J = 14.7, 6.8 Hz, 2H), 1.43 (t, J = 7.2 Hz, 3H), 0.98 (t, J = 7.9 Hz, 11H), 0.76 (q, J = 7.9 Hz, 8H). HPLC and high-resolution mass spectrometry were used to analyze the quality of the synthesized TESO-Linker.

Chromatography analysis to determine efficiency of the desilylation reaction [077] TESO-Coumarin, TBSO-Coumarin and TIPSO-Coumarin (150 μM) were treated with [078] Phe-BF<sub>3</sub> (150 µM) in PBS (including 5% DMSO) at 37°C. HPLC analysis was performed at 5 and 240 min after incubation (Fig. 1d, e). For bioorthogonality evaluation (Fig. 1f), TESO-Coumarin (150 µM) was treated with H<sub>2</sub>O<sub>2</sub>, GSH or other biologically relevant anions, including Cl<sup>-</sup>, I<sup>-</sup>, NO<sub>3</sub><sup>-</sup>, PO<sub>4</sub><sup>3-</sup>, SO<sub>4</sub><sup>2-</sup> (150 µM) in PBS (including 5% DMSO) at 37°C. HPLC analysis was performed at 240 min after incubation. To compare the reaction efficiency of Phe-BF<sub>3</sub> with those of other fluorine donors (Fig. 1g), TESO-Coumarin (150 μM) was treated with Phe-BF<sub>3</sub> or another organofluorine in PBS (including 5% DMSO) at 37°C. HPLC analysis was performed at 240 min after incubation. Agilent Eclipse XDB-C18 5 µm 4.6 x 250 mm analytical column was used for the HPLC analyses, and leflunomide ( $c = 20 \mu M$ ) was added as the internal standard. Solvent A: water (0.1% TFA); solvent B: MeCN; 0 to 2 min: 5% B, 2 to 10 min: 5% to 95% B, 10 to 15 min: 95% B, 15 to 17 min: 95% to 5% B; flow rate: 0.6 mL/min; column temperature: 19 to 21°C. The reaction yields were determined by HPLC peak integration at the given wavelength (254 nm). All the measurements were performed in triplicates and the average numbers are shown.

## [079] Radiochemistry and PET imaging

[080] [18F]Phe-BF<sub>3</sub> are radiosynthesized via the one-step <sup>18</sup>F-<sup>19</sup>F isotope exchange (IEX) reaction. The labeling method and purification procedure have been described previously<sup>36,37</sup>. PET scans were obtained and images analysis were performed using a Mediso 122s PET scanner. About 3.7 MBq of [18F]Phe-BF<sub>3</sub> and [89Zr]Zr-labeled protein-NP conjugates were administrated via tail-vein injection under isoflurane anesthesia. Standard data acquisition and image reconstruction of the PET data were performed.

## [081] Preparation of DBCO-PEG decorated NPs (DBCO-PEG-NPs)

[082] The water-soluble spherical gold nanoparticles (NPs) (A68095) were generated by 3A Chemicals. PEG-decorated NPs were prepared according to the published methods <sup>77,78</sup>. Briefly, a solution of NPs (60 nm) containing citric acid was centrifuged at 14,000 g for 5 min, decanted, and resuspended in water to remove excess citric acid. 10 µL of 8 mM DBCO-PEG3400-SH were added to 1 mL of 1 mg/mL NPs solution. The mixture was stirred for 30 min at RT, and 200 µL of 10 mM MeO-PEG5000-SH were then added, stirring for 24 h at 4°C. The reaction crudes were centrifuged at 14,000 g for 5 min, decanted, and resuspended in water to remove excess PEG. The size of the DBCO-PEG-NPs was confirmed by transmission electron microscopy.

## [083] Preparation of NP\_GFP, NP\_mNeonGreen-NLS and NP\_GA3 materials

[084] The desired NP-protein conjugates were prepared by following the previous publications  $^{79,80}$ . Briefly, to obtain NP\_GFP and NP\_mNeonGreen-NLS, 100  $\mu L$  of N3-OTES-maleimide linker (Compound 7, TESO-Linker) (PBS, 500  $\mu M$ ) was added to 100  $\mu L$  of GFP or mNeonGreen-NLS solution (PBS, 100  $\mu M$ ) at 4°C for 24 h. Excess linker was removed from the solution by ultrafiltration centrifugation for 4 times and to modified GFP or mNeonGreen-NLS protein were obtained. 100  $\mu L$  of the modified proteins (20  $\mu M$ ) were reacted with 100  $\mu L$  of DBCO-PEG-NPs solutions (200  $\mu M$ ) with stirring at RT for 30 min. After overnight storage at 4°C, the reaction was centrifuged at 5,000 g for 5 min, decanted, and resuspended in water to remove excess un-conjugated proteins. To prepare NP\_GA3, all operations were carried out at 4°C. 100  $\mu L$  of N3-OTES-maleimide linker (PBS, 500  $\mu M$ ) was added slowly to 100  $\mu L$  of the (N+C) nonvalent complex of GSDMA3 (60  $\mu M$ ) solution, and the reaction proceeded for 6 h. Excess linker was removed by overnight dialysis. After centrifugation to remove the precipitate, the modified GA3 protein was obtained and resuspended in PBS. 100  $\mu L$  of the modified GA3 protein (20  $\mu M$ ) was incubated with 100  $\mu L$  of DBCO-PEG-NPs solutions (200  $\mu M$ ) for 6 h. The mixture was used directly to treat cells or mice.

## [085] Cell culture and transfection

[086] HeLa and mouse EMT6 and CT26 cells were obtained from the American Type Culture Collection (ATCC). Mouse mammary carcinoma 4T1 cells were obtained from the China Infrastructure of Cell Line Resources (Chinese Academy of Medical Sciences, Beijing, China). Primary bone marrow-derived macrophage (priBMDM) cells were prepared and cultured by following a standard protocol as previously described<sup>4</sup>. The cells are frequently checked by virtue of their morphological features and functionalities, but have not been subjected to authentication by short tandem repeat (STR) profiling. All cell lines were tested for mycoplasma regularly by the commonly used PCR strategy. 4T1, EMT6, CT26 and priBMDM cells were

cultured in RIPM 1640 medium and HeLa cells were cultured in Dulbecco's modified Eagle's medium (DMEM). The media were supplemented with 10% (vol/vol) fetal bovine serum (FBS) and 2 mM L-glutamine. All cells were cultured in a 5% CO<sub>2</sub> incubator at 37°C. Transient transfection was performed with the JetPRIME (Polyplus Transfection) by following the manufacturer's instructions. GA3-FL or the GA3-(N+C) proteins were electroporated into CT26 cells using the Neon Transfection System (Life Technologies).

#### [087] Immunostaining and fluorescence microscopy

[088] Frozen 4T1 tumor sections were used for anti-CD3 immunostaining. At the end of indicated treatments on day 16, 4T1 tumors were dissected from mice and embedded into Cryomold moulds filled with the OCT compound (SAKURA 4583). The tissue samples were frozen on dry ice for 30 min and stored at -20°C. For immunostaining, the frozen tumor tissues were sectioned into 10-µm pieces using cryostat (Lecia CM1950) and mounted on slides. After washing out the OCT with PBS, the slices were fixed with 4% paraformaldehyde for 30 min and then blocked and permeabilized with PBS containing 1% FBS and 0.2% Triton X-100 for 1 h. The slides were stained with PE-conjugated anti-mouse CD3 antibody for 1 h and Hoechst for 1 min. Zeiss LSM800 confocal laser scanning microscope was used to acquire images on the 10x or 40x objectives.

[089] The 4T1 tumor model was used for quantifying Phe-BF<sub>3</sub>-mediated release of mNeonGreen-NLS from NP\_ mNeonGreen-NLS. The NP\_mNeonGreen-NLS conjugates were administrated into 4T1 tumor-bearing mice through intravenous injections on day 6, 9 and 12 followed by intravenous injections of Phe-BF<sub>3</sub> on day 7, 8, 10, 11, 13, and 14. On day 15, mice were sacrificed and tumors were dissected from the surrounding fascia, embedded and frozen in the Cryomold moulds filled with the OCT compound. Processing of the tumor tissue was performed as above described for anti-CD3 staining and the slides were stained with Alexa Fluor 647-conjugated phalloidin (A22287, Thermo Fisher Scientific Inc.). Zeiss LSM850 confocal microscope was used to record the images on a 60x oil objective.

## [090] Cell pyroptosis assays

[091] HeLa, EMT6, 4T1, and priBMDM cells were seeded into a 6 or 96-well plate 24 h before subjected to indicated treatments. To examine cell morphology, static bright field images of pyroptotic cells were captured using an Olympus IX71 microscope. The image data shown are representative of at least three randomly selected fields. For flow cytometry analysis, all cells in each 6-wel plate were collected and washed twice with PBS, stained by using the Annexin V-FITC/PI staining kit (Abmaking) (Annexin V-FITC for 10 min and PI for 5 min). The sample volume was increased to 500 μl with adding more PBS and the samples were

analyzed on a BD FACS Aria III flow cytometer. Data were processed using FlowJo software. Cell viability was determined by using the CellTiter-Glo Luminescent Cell Viability Assay (Promega).

#### [092] Purification of recombinant proteins

To obtain engineered GSDMA3 protein containing the PreScission protease (PPase) cleavage site and the mNeonGreen-NLS proteins, E. coli BL21 (DE3) cells harboring pET28a-6×His-SUMO-GSDMA3 or mNeonGreen-NLS were grown in Luria-Bertani (LB) media supplemented with 30 µg/ml kanamycin. After OD<sub>600</sub> of the culture reached 0.8, 0.4 mM isopropyl-B-D-thiogalactopyranoside (IPTG) was added to induce protein expression at 18°C overnight. Bacteria were harvested and sonicated in the lysis buffer containing 20 mM Tris-HCl (pH 8.0), 150 mM NaCl, 20 mM imidazole and 10 mM 2-mercaptoethanol. The fusion protein was first affinity-purified by Ni-Sepharose beads (GE Healthcare Life Sciences). The homemade ULP-1 protease was used to remove the 6×His-SUMO tag by overnight cleavage at 4°C. HiTrap O ion-exchange and Superdex G75 gel-filtration chromatography (GE Healthcare Life Sciences) were then performed sequentially for further purification. To obtain the gasdermin-N and -C (N+C) noncovalent complex of GSDMA3, the purified engineered GSDMA3 protein was digested overnight with homemade PPase at 4°C. The (N+C) complex of GSDMA3 was further purified by Superdex G75 gel-filtration chromatography in the absence of reductants. 2mercaptoethanol present in the mNeonGreen-NLS protein was also removed at Superdex G75 gel-filtration chromatography step.

#### [094] Stimulation of cells with NP-protein conjugates and Phe-BF<sub>3</sub>

[095] HeLa, EMT6, 4T1, and priBMDM cells, seeded in 6-well plates, were treated with the NP\_GA3 conjugates for 24 h. Subsequently, the NP\_GA3-containing media were replaced with Phe-BF<sub>3</sub>-containing media and incubated for another 24 h. The cells were then subjected to flow cytometry analyses. For confocal microscopy imaging assay of GFP release from NP\_GFP, priBMDM cells were seeded onto glass coverslips in 24-well plates and treated sequentially with the NP\_GFP conjugate for 24 h and Phe-BF<sub>3</sub> for another 24 h. The treated cells were washed with PBS and fixed with 4% paraformaldehyde. Nucleus was stained with Hoechst. Fluorescence images were captured by using the Zeiss LSM800 confocal microscope on a 20x objective.

## [096] In vivo PI staining assay of tumor cell pyroptosis

**[097]** For propidium iodide (PI) labeling of pyroptotic cells *in vivo*, 4T1 tumor-bearing mice were administrated with PI (2.5 mg/kg) via intravenous injection at 24 h after the last round of NP\_GA3+PheBF<sub>3</sub> treatment (Fig. 4b). 10 min later, the mice were sacrificed and the tumors

were harvested, placed and frozen into the OCT-containing Cryomold moulds. After slicing and mounting, the slides were scanned directly and immediately on the Zeiss LSM800 confocal microscope.

## [098] Tumor model and FACS analyses of tumor-infiltrating lymphocytes

All mice used were purchased from the Vital River Laboratories. To construct the tumor [099] model, 4T1 (1 x 10<sup>6</sup>) or EMT6 (2 x 10<sup>6</sup>) cells in 100 µl of PBS were implanted into the right flank of BALB/c female mice (6-8 weeks old). Mice were intravenously injected with NP\_GA3 or an indicated control on day 6, 9, and 12, and each of the three treatments was followed by two intravenous injections of Phe-BF<sub>3</sub> (on day 7, 8, 10, 11, 13, and 14), as illustrated in Fig. 4b. For the combinatory therapy in Fig. 5g-j, anti-PD1 antibody (5 mg/kg) was intraperitoneally injected into the mice on day 9, 11, 13 and 15 after a single round of NP\_GA3+PheBF<sub>3</sub> treatment from day 6-8. When the tumor was palpable, its long diameter (L) and short diameter (W) were measured every 3-5 days with a caliper; the tumor volume was determined using the volume formula for an ellipsoid (i.e.,  $1/2 \times L \times W^2$ ). Mice were sacrificed with CO<sub>2</sub> inhalation when the tumor reached 2,000 mm<sup>3</sup>. The same protocol was used to construct 4T1 tumor model in the Nu/Nu mice. For FACS of tumor-infiltrating lymphocytes, tumors were harvested on day 16 after inoculation. The tumors were dissected from the surrounding fascia, weighted, minced into pieces by sterile scissors, and grinded. Cell clumps were removed through a 70-um cell strainer to obtain sing-cell suspensions. The suspension was centrifuged and the cell pellets were washed twice with PBS containing 1% BSA (FACS buffer). Lymphocytes were isolated by Percoll density gradient centrifugation, washed and resuspended in the FACS buffer, blocked with anti-mouse CD16/CD32 (clone 93, BioLegend) for 30 min, and finally stained with the indicated antibodies for another 1 h. The LIVE/DEAD Fixable Near-IR Dead Cell Stain Kit (L10119, Invitrogen) was used to determine cell viability during FACS analysis. The Foxp3 Fixation/Permeabilization Kit (00-5521-00, Invitrogen) was used to stain the intracellular Foxp3 by following the manufacturer's instructions.

## [0100] Single-cell RNA sequencing (scRNA-Seq)

[0101] The tumor-infiltrating lymphocytes isolated above were stained with PE-conjugated anti-mouse CD45 antibody (clone 30-F11, Biolegend). CD45<sup>+</sup> immune cells were then enriched by using a BD FACS Aria III flow cytometer. Cell viability was monitored in real time during preparation of the single CD45<sup>+</sup> immune cells suspension. 10,000 cells (~ 600 single cells/µl) from each experimental group were barcoded and pooled using the 10x Genomics device. Samples were prepared following the manufacturer's protocol and sequenced on an Illumina NextSeq sequencer. The Cell Ranger analysis pipeline (v3.0.2) was used for sample de-

multiplexing, barcode processing, alignment, filtering, UMI counting, and aggregation of the sequencing runs. For quality control of the scRNA-Seq procedure, cells with less than 300 genes detected as well as cells whose transcript counts for mitochondria-encoded genes were more than 15% of the total transcript counts were removed from subsequent analyses. Genes detected in fewer than three cells across the data set were also excluded, yielding a preliminary expression matrix of 18,069 cells. After obtaining the digital gene expression (DGE) data matrix, Seurat (v3.0.0.9000) was used for dimension reduction, clustering, and differential gene expression analyses.

## [0102] Immune cell depletion

[0103] Each tumor-bearing mouse was intraperitoneally administrated with 200 µg of antimouse CD4, anti-mouse CD8, or the isotype control antibody at day 5, 8, 11, and 14 after inoculation of the 4T1 cells. To verify the depletion efficiency, the percentage of CD4<sup>+</sup> or CD8<sup>+</sup> T lymphocytes in the spleen was determined on day 16 by using a BD FACSAria III flow cytometer.

#### [0104] General protocols of animal studies

[0105] The tumor-bearing mice were subjected to indicated treatments and small-animal PET studies when the tumor volume reached 100 mm<sup>3</sup> (about 1 week after inoculation) and 100-300 mm<sup>3</sup> (2-3 weeks after inoculation), respectively.

### [0106] References

- [0107] 1 Patterson, D. M. & Prescher, J. A. Orthogonal bioorthogonal chemistries. *Current Opinion in Chemical Biology* 28, 141-149 (2015).
- [0108] 2 Li, J. & Chen, P. R. Development and application of bond cleavage reactions in bioorthogonal chemistry. *Nature Chemical Biology* 12, 129 (2016).
- [0109] 3 Kayagaki, N. *et al.* Caspase-11 cleaves gasdermin D for non-canonical inflammasome signalling. *Nature* 526, 666-671 (2015).
- [0110] 4 Shi, J. *et al.* Cleavage of GSDMD by inflammatory caspases determines pyroptotic cell death. *Nature* 526, 660 (2015).
- [0111] 5 Aglietti, R. A. *et al.* GsdmD p30 elicited by caspase-11 during pyroptosis forms pores in membranes. *Proc Natl Acad Sci U S A* 113, 7858-7863 (2016).
- [0112] 6 Ding, J. *et al.* Pore-forming activity and structural autoinhibition of the gasdermin family. *Nature* 535, 111-116 (2016).
- [0113] 7 Liu, X. *et al.* Inflammasome-activated gasdermin D causes pyroptosis by forming membrane pores. *Nature* 535, 153-158 (2016).

[0114] 8 Sborgi, L. *et al.* GSDMD membrane pore formation constitutes the mechanism of pyroptotic cell death. *EMBO J* 35, 1766-1778 (2016).

- [0115] 9 Shi, J., Gao, W. & Shao, F. Pyroptosis: Gasdermin-Mediated Programmed Necrotic Cell Death. *Trends Biochem Sci* 42, 245-254 (2017).
- [0116] 10 Pattabiraman, D. R. *et al.* Activation of PKA leads to mesenchymal-to-epithelial transition and loss of tumor-initiating ability. *Science* 351, aad3680 (2016).
- [0117] 11 Row, R. D. & Prescher, J. A. Constructing New Bioorthogonal Reagents and Reactions. *Accounts of Chemical Research* 51, 1073-1081 (2018).
- [0118] 12 Yang, M., Li, J. & Chen, P. R. Transition metal-mediated bioorthogonal protein chemistry in living cells. *Chemical Society Reviews* 43, 6511-6526 (2014).
- [0119] 13 Li, J. *et al.* Palladium-triggered deprotection chemistry for protein activation in living cells. *Nature Chemistry* 6, 352 (2014).
- [0120] 14 Lin, L. *et al.* Carbon nanotube-assisted optical activation of TGF- $\beta$  signalling by near-infrared light. *Nature Nanotechnology* 10, 465 (2015).
- [0121] 15 Shaffer, T. M., Pratt, E. C. & Grimm, J. Utilizing the power of Cerenkov light with nanotechnology. *Nature Nanotechnology* 12, 106 (2017).
- [0122] 16 Yao, Q. *et al.* Synergistic enzymatic and bioorthogonal reactions for selective prodrug activation in living systems. *Nature Communications* 9, 5032 (2018).
- [0123] 17 Rossin, R. *et al.* Chemically triggered drug release from an antibody-drug conjugate leads to potent antitumour activity in mice. *Nature Communications* 9, 1484 (2018).
- [0124] 18 Liu, Z. *et al.* An organotrifluoroborate for broadly applicable one-step 18F-labeling. *Angew Chem Int Ed Engl* 53, 11876-11880 (2014).
- [0125] 19 Bernard-Gauthier, V. *et al.* Recent Advances in 18F Radiochemistry: A Focus on B-18F, Si-18F, Al-18F, and C-18F Radiofluorination via Spirocyclic Iodonium Ylides. *Journal of Nuclear Medicine* 59, 568-572 (2018).
- [0126] 20 Sun, X. et al. Peptide-based imaging agents for cancer detection. Advanced Drug Delivery Reviews 110-111, 38-51 (2017).
- [0127] 21 Grootjans, W. et al. PET in the management of locally advanced and metastatic NSCLC. *Nature Reviews Clinical Oncology* 12, 395 (2015).
- [0128] 22 Maurer, T., Eiber, M., Schwaiger, M. & Gschwend, J. E. Current use of PSMA–PET in prostate cancer management. *Nature Reviews Urology* 13, 226 (2016).

[0129] 23 Zhao, Y. & Shao, F. Diverse mechanisms for inflammasome sensing of cytosolic bacteria and bacterial virulence. *Curr Opin Microbiol* 29, 37-42 (2016).

- [0130] 24 Rathinam, V. A. K., Zhao, Y. & Shao, F. Innate immunity to intracellular LPS. *Nat Immunol* 20, 527-533 (2019).
- [0131] 25 Broz, P. & Dixit, V. M. Inflammasomes: mechanism of assembly, regulation and signalling. *Nat Rev Immunol* 16, 407-420 (2016).
- [0132] 26 Bergsbaken, T., Fink, S. L. & Cookson, B. T. Pyroptosis: host cell death and inflammation. *Nat Rev Microbiol* 7, 99-109 (2009).
- [0133] 27 Jorgensen, I., Rayamajhi, M. & Miao, E. A. Programmed cell death as a defence against infection. *Nat Rev Immunol* 17, 151-164 (2017).
- [0134] 28 Rogers, C. *et al.* Cleavage of DFNA5 by caspase-3 during apoptosis mediates progression to secondary necrotic/pyroptotic cell death. *Nat Commun* 8, 14128 (2017).
- [0135] 29 Wang, Y. *et al.* Chemotherapy drugs induce pyroptosis through caspase-3 cleavage of a gasdermin. *Nature* 547, 99 (2017).
- [0136] 30 Galluzzi, L. *et al.* Molecular mechanisms of cell death: recommendations of the Nomenclature Committee on Cell Death 2018. *Cell Death Differ* 25, 486-541 (2018).
- [0137] 31 Ruan, J., Xia, S., Liu, X., Lieberman, J. & Wu, H. Cryo-EM structure of the gasdermin A3 membrane pore. *Nature* 557, 62-67 (2018).
- [0138] 32 Man, S. M., Karki, R. & Kanneganti, T. D. Molecular mechanisms and functions of pyroptosis, inflammatory caspases and inflammasomes in infectious diseases. *Immunol Rev* 277, 61-75 (2017).
- [0139] 33 Evavold, C. L. *et al.* The Pore-Forming Protein Gasdermin D Regulates Interleukin-1 Secretion from Living Macrophages. *Immunity* 48, 35-44 e36 (2018).
- [0140] 34 Heilig, R. *et al.* The Gasdermin-D pore acts as a conduit for IL-1beta secretion in mice. *Eur J Immunol* 48, 584-592 (2018).
- [0141] 35 Liu, Z. *et al.* Preclinical evaluation of a high-affinity 18F-trifluoroborate octreotate derivative for somatostatin receptor imaging. *J Nucl Med* 55, 1499-1505 (2014).
- [0142] 36 Liu, Z. *et al.* One-step (18)F labeling of biomolecules using organotrifluoroborates. *Nat Protoc* 10, 1423-1432 (2015).
- [0143] 37 Liu, Z. et al. Boramino acid as a marker for amino acid transporters. Sci Adv 1, e1500694 (2015).

[0144] 38 Li, C., Liu, H., Duan, D., Zhou, Z. & Liu, Z. Preclinical study of an 18F-labeled glutamine derivative for cancer imaging. *Nuclear Medicine and Biology* 64-65, 34-40 (2018).

- [0145] 39 Kommidi, H. *et al.* An [(18)F]-Positron-Emitting, Fluorescent, Cerebrospinal Fluid Probe for Imaging Damage to the Brain and Spine. *Theranostics* 7, 2377-2391 (2017).
- [0146] 40 Kommidi, H. *et al.* (18)F-Positron Emitting/Trimethine Cyanine-Fluorescent Contrast for Image-Guided Prostate Cancer Management. *J Med Chem* 61, 4256-4262 (2018).
- [0147] 41 Corey, E. J. & Venkateswarlu, A. Protection of hydroxyl groups as tert-butyldimethylsilyl derivatives. *Journal of the American Chemical Society* 94, 6190-6191 (1972).
- [0148] 42 David Crouch, R. Selective monodeprotection of bis-silyl ethers. *Tetrahedron* 60, 5833-5871 (2004).
- [0149] 43 Liu, G. *et al.* Hyperbranched Self-Immolative Polymers (hSIPs) for Programmed Payload Delivery and Ultrasensitive Detection. *J Am Chem Soc* 137, 11645-11655 (2015).
- [0150] 44 Sella, E. & Shabat, D. Dendritic chain reaction. *J Am Chem Soc* 131, 9934-9936 (2009).
- [0151] 45 Nelson, T. D. & Crouch, R. D. Selective Deprotection of Silyl Ethers. *Synthesis* 1996, 1031-1069 (1996).
- [0152] 46 Liu, Z. *et al.* From minutes to years: predicting organotrifluoroborate solvolysis rates. *Chemistry* 21, 3924-3928 (2015).
- [0153] 47 Pilcher, A. S. & DeShong, P. Utilization of Tetrabutylammonium Triphenyldifluorosilicate as a Fluoride Source for Silicon-Carbon Bond Cleavage. *J Org Chem* 61, 6901-6905 (1996).
- [0154] 48 Handy, C. J., Lam, Y. F. & DeShong, P. On the synthesis and NMR analysis of tetrabutylammonium triphenyldifluorosilicate. *J Org Chem* 65, 3542-3543 (2000).
- [0155] 49 Lee, E. *et al.* A Fluoride-Derived Electrophilic Late-Stage Fluorination Reagent for PET Imaging. *Science* 334, 639 (2011).
- [0156] 50 Phillips, E. *et al.* Clinical translation of an ultrasmall inorganic optical-PET imaging nanoparticle probe. *Science Translational Medicine* 6, 260ra149 (2014).
- [0157] 51 Erathodiyil, N. & Ying, J. Y. Functionalization of inorganic nanoparticles for bioimaging applications. *Acc Chem Res* 44, 925-935 (2011).
- [0158] 52 Papasani, M. R., Wang, G. & Hill, R. A. Gold nanoparticles: the importance of physiological principles to devise strategies for targeted drug delivery. *Nanomedicine* 8, 804-814 (2012).

[0159] 53 Wilhelm, S. *et al.* Analysis of nanoparticle delivery to tumours. *Nature Reviews Materials* 1, 16014 (2016).

- [0160] 54 Blanco, E., Shen, H. & Ferrari, M. Principles of nanoparticle design for overcoming biological barriers to drug delivery. *Nature Biotechnology* 33, 941 (2015).
- [0161] 55 Chithrani, D. B. Intracellular uptake, transport, and processing of gold nanostructures. *Mol Membr Biol* 27, 299-311 (2010).
- [0162] 56 Swierczewska, M., Lee, S. & Chen, X. The design and application of fluorophore–gold nanoparticle activatable probes. *Physical Chemistry Chemical Physics* 13, 9929-9941 (2011).
- [0163] 57 Perrin, D. M. [18F]-Organotrifluoroborates as Radioprosthetic Groups for PET Imaging: From Design Principles to Preclinical Applications. *Accounts of Chemical Research* 49, 1333-1343 (2016).
- [0164] 58 Dias, G. M. *et al.* 89Zr for antibody labeling and in vivo studies A comparison between liquid and solid target production. *Nuclear Medicine and Biology* 58, 1-7 (2018).
- [0165] 59 Rodriguez, E. A. *et al.* The Growing and Glowing Toolbox of Fluorescent and Photoactive Proteins. *Trends Biochem Sci* 42, 111-129 (2017).
- [0166] 60 Borst, J., Ahrends, T., Babala, N., Melief, C. J. M. & Kastenmuller, W. CD4(+) T cell help in cancer immunology and immunotherapy. *Nat Rev Immunol* 18, 635-647 (2018).
- [0167] 61 Wang, J. et al. Fibrinogen-like Protein 1 Is a Major Immune Inhibitory Ligand of LAG-3. Cell 176, 334-347 e312 (2019).
- [0168] 62 Chaput, N. *et al.* Regulatory T cells prevent CD8 T cell maturation by inhibiting CD4 Th cells at tumor sites. *J Immunol* 179, 4969-4978 (2007).
- [0169] 63 Zou, W., Wolchok, J. D. & Chen, L. PD-L1 (B7-H1) and PD-1 pathway blockade for cancer therapy: Mechanisms, response biomarkers, and combinations. *Sci Transl Med* 8, 328rv324 (2016).
- [0170] 64 Ribas, A. & Wolchok, J. D. Cancer immunotherapy using checkpoint blockade. *Science* 359, 1350-1355 (2018).
- [0171] 65 Sharma, P., Hu-Lieskovan, S., Wargo, J. A. & Ribas, A. Primary, Adaptive, and Acquired Resistance to Cancer Immunotherapy. *Cell* 168, 707-723 (2017).
- [0172] 66 Sharma, P. & Allison, J. P. The future of immune checkpoint therapy. *Science* 348, 56-61 (2015).

[0173] 67 Tumeh, P. C. *et al.* PD-1 blockade induces responses by inhibiting adaptive immune resistance. *Nature* 515, 568-571 (2014).

- [0174] 68 Schwartz, H. S. & Grindey, G. B. Adriamycin and daunorubicin: a comparison of antitumor activities and tissue uptake in mice following immunosuppression. *Cancer Res* 33, 1837-1844 (1973).
- [0175] 69 Casares, N. *et al.* Caspase-dependent immunogenicity of doxorubicin-induced tumor cell death. *J Exp Med* 202, 1691-1701 (2005).
- [0176] 70 Krysko, D. V. et al. Immunogenic cell death and DAMPs in cancer therapy. Nat Rev Cancer 12, 860-875 (2012).
- [0177] 71 Galluzzi, L., Buque, A., Kepp, O., Zitvogel, L. & Kroemer, G. Immunogenic cell death in cancer and infectious disease. *Nat Rev Immunol* 17, 97-111 (2017).
- [0178] 72 Yatim, N. *et al.* RIPK1 and NF-kappaB signaling in dying cells determines cross-priming of CD8(+) T cells. *Science* 350, 328-334 (2015).
- [0179] 73 Aaes, T. L. *et al.* Vaccination with Necroptotic Cancer Cells Induces Efficient Anti-tumor Immunity. *Cell Rep* 15, 274-287 (2016).
- [0180] 74 Wang, W. *et al.* CD8(+) T cells regulate tumour ferroptosis during cancer immunotherapy. *Nature* 569, 270-274 (2019).
- [0181] 75 Kearney, C. J. *et al.* Necroptosis suppresses inflammation via termination of TNF- or LPS-induced cytokine and chemokine production. *Cell Death Differ* 22, 1313-1327 (2015).
- [0182] 76 Brouckaert, G. *et al.* Phagocytosis of necrotic cells by macrophages is phosphatidylserine dependent and does not induce inflammatory cytokine production. *Mol Biol Cell* 15, 1089-1100 (2004).
- [0183] 77 Cheng, Y. *et al.* Highly efficient drug delivery with gold nanoparticle vectors for in vivo photodynamic therapy of cancer. *J Am Chem Soc* 130, 10643-10647 (2008).
- [0184] 78 Duncan, B., Kim, C. & Rotello, V. M. Gold nanoparticle platforms as drug and biomacromolecule delivery systems. *J Control Release* 148, 122-127 (2010).
- [0185] 79 De, M. *et al.* Sensing of proteins in human serum using conjugates of nanoparticles and green fluorescent protein. *Nat Chem* 1, 461-465 (2009).
- [0186] 80 Rana, S., Yeh, Y. C. & Rotello, V. M. Engineering the nanoparticle-protein interface: applications and possibilities. *Curr Opin Chem Biol* 14, 828-834 (2010).

#### **CLAIMS**

 A method of inducing an antitumor immune response in a person in need thereof, comprising: administering to the person a pyroptosis activator; and detecting a resultant pyroptosis-induced antitumor immune response.

2. The method of claim 1 further comprising:

administering to the person an anti-PD1 therapeutic wherein the pyroptosis activator and the anti-PD1 therapeutic synergistically induce tumor regression in the person; and detecting a resultant tumor regression in the person.

- 3. The method of claim 1 or 2 wherein the pryoptosis activator is a gasdermin agonist.
- 4. The method of claim 1 or 2 wherein the pyroptosis activator is a bioothogonal agent that releases an activationally restrained gasdermin in tumor cells of the person.
- 5. The method of claim 1, 2 or 3 wherein the pyroptosis activator is a bioothogonal agent that releases an activationally restrained gasdermin in tumor cells of the person, wherein the gasdermin is conjugated to a matrix (such as a nanoparticle) in the cells, and the biothorganal agent releases (deconjugates) the gasdermin from the matrix.
- 6. The method of claim 4 or 5 wherein the gasdermin is activationally restrained though a silyl ether linkage, and the agent is an organotrifluoroborate that cleaves the linkage and thereby releases the gasdermin from activational restraint.
- 7. The method of claim 6 wherein the linker comprises an ortho-carbamoylmethylene silyl-phenolic ether, in which the carbamate carbon is linked to the gasdermin.
- 8. The method of claim 6 or 7 wherein the ortho-carbamoylmethylene silyl-phenolic ether comprises a silyl ether moiety selected from:

```
trimethylsilyl ether (TMS),
triethylsilyl ether (TES),
tert-butyldimethylsilyl ether (TBS/TBDMS),
tert-butyldiphenylsilyl ether (TBDPS), and
triisopropylsilyl ether (TIPS).
```

9. The method of claim 6, 7 or 8 wherein the organotrifluoroborate comprises a boroamino acid (BAA), e.g. PheBF3.

- 10. The method of claim 4, 5, 6, 7, 8 or 9 wherein the activationally restrained gasdermin is conjugated to a nanoparticle (NP).
- 11. A method for releasing in a cell a client molecule from a silyl ether containing linker, comprising:

introducing into the cell an organotrifluoroborate under conditions wherein the organotrifluoroborate reacts with the silyl ether to desilylate and release from the linker the client molecule; and optionally,

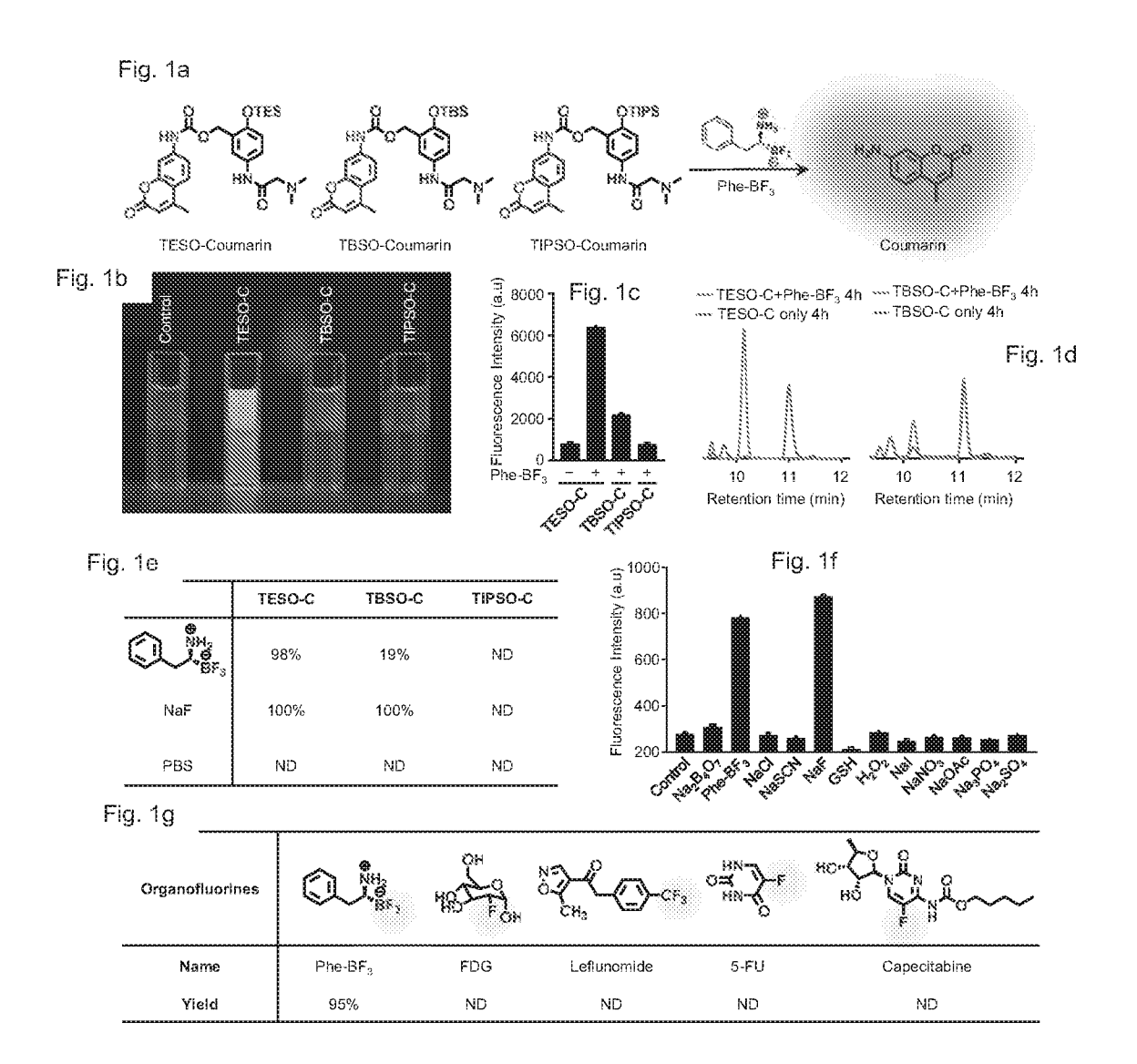
detecting resultant release of the client molecule.

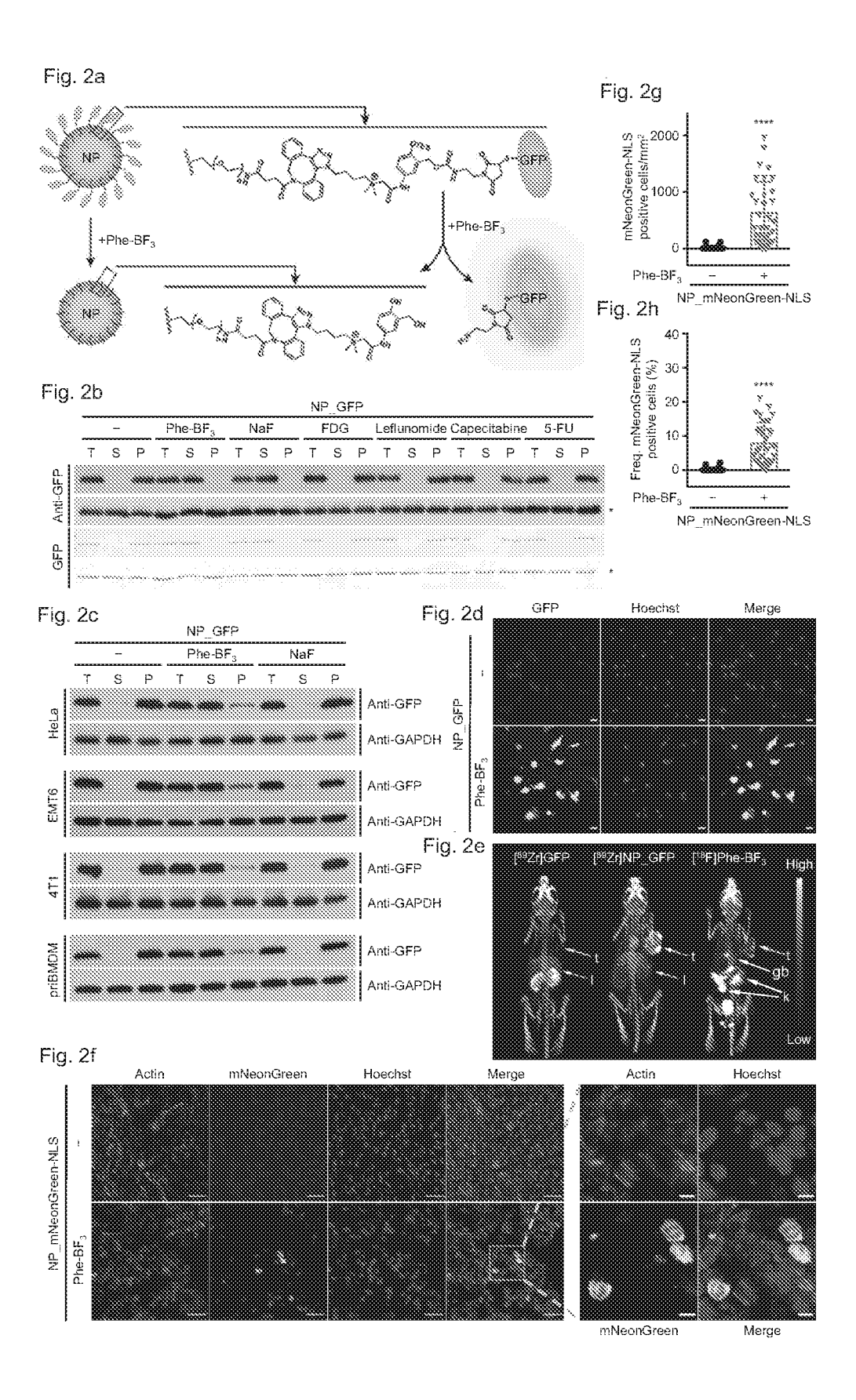
- 12. The method of claim 11 wherein the linker comprises an ortho-carbamoylmethylene silylphenolic ether, in which the carbamate carbon is linked to the client molecule.
- 13. The method of claim 11 or 12 wherein the linker comprises a silyl ether that is trimethylsilyl ether (TMS), triethylsilyl ether (TES), tert-butyldimethylsilyl ether (TBS/TBDMS), tert-butyldiphenylsilyl ether (TBDPS), or triisopropylsilyl ether (TIPS).
- 14. The method of claim 11, 12 or 13 wherein the linker is joined to a nanoparticle.
- 15. The method of claim 11, 12, 13 or 14 wherein the organotrifluoroborate comprises a boroamino acid (BAA), e.g. PheBF3.
- 16. The method of claim 11, 12, 13, 14 or 15 wherein the client molecule is a label (e.g. GFP), a cytotoxic drug (e.g. imatinib, pemetrexed), or a tumor suppressor protein (e.g. gasdermin).
- 17. The method of claim 11, 12, 13, 14, 15 or 16 wherein the cell is a cancer cell.
- 18. The method of claim 11, 12, 13, 14, 15, 16 or 17 wherein the linker is joined to a nanoparticle, the client molecule is a gasdermin, the cell is a cancer cell of a tumor, and the method activates the gasdermin in the cell to stimulate pyroptosis in the cell and achieve anti-tumor immunotherapy.

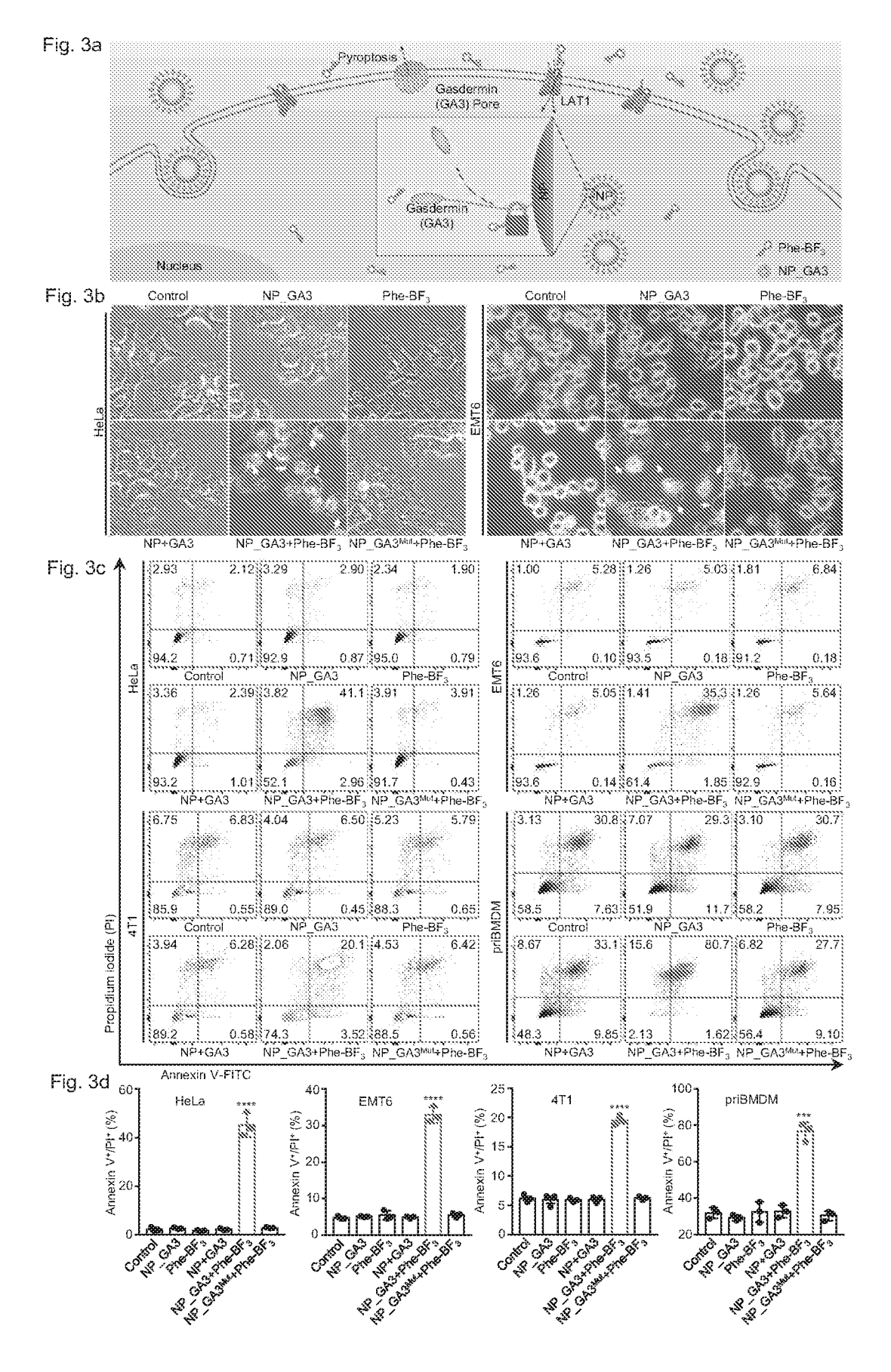
19. The method of claim 18 wherein the introducing step comprises administering the organotrifluoroborate to a person in need of anti-tumor immunotherapy, and optionally detecting a resultant pyroptosis-induced antitumor immune response.

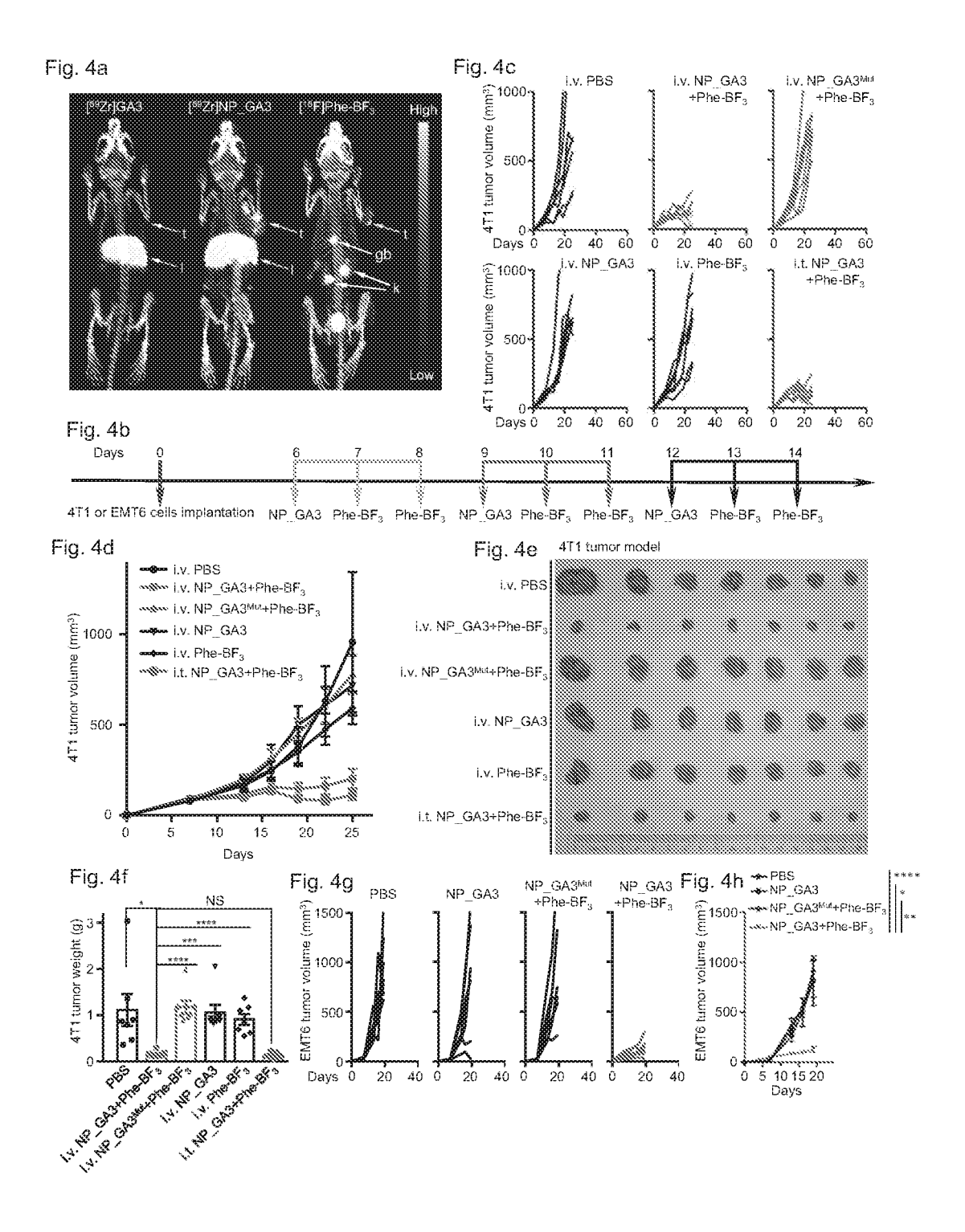
20. The method of claim 19 further comprising:

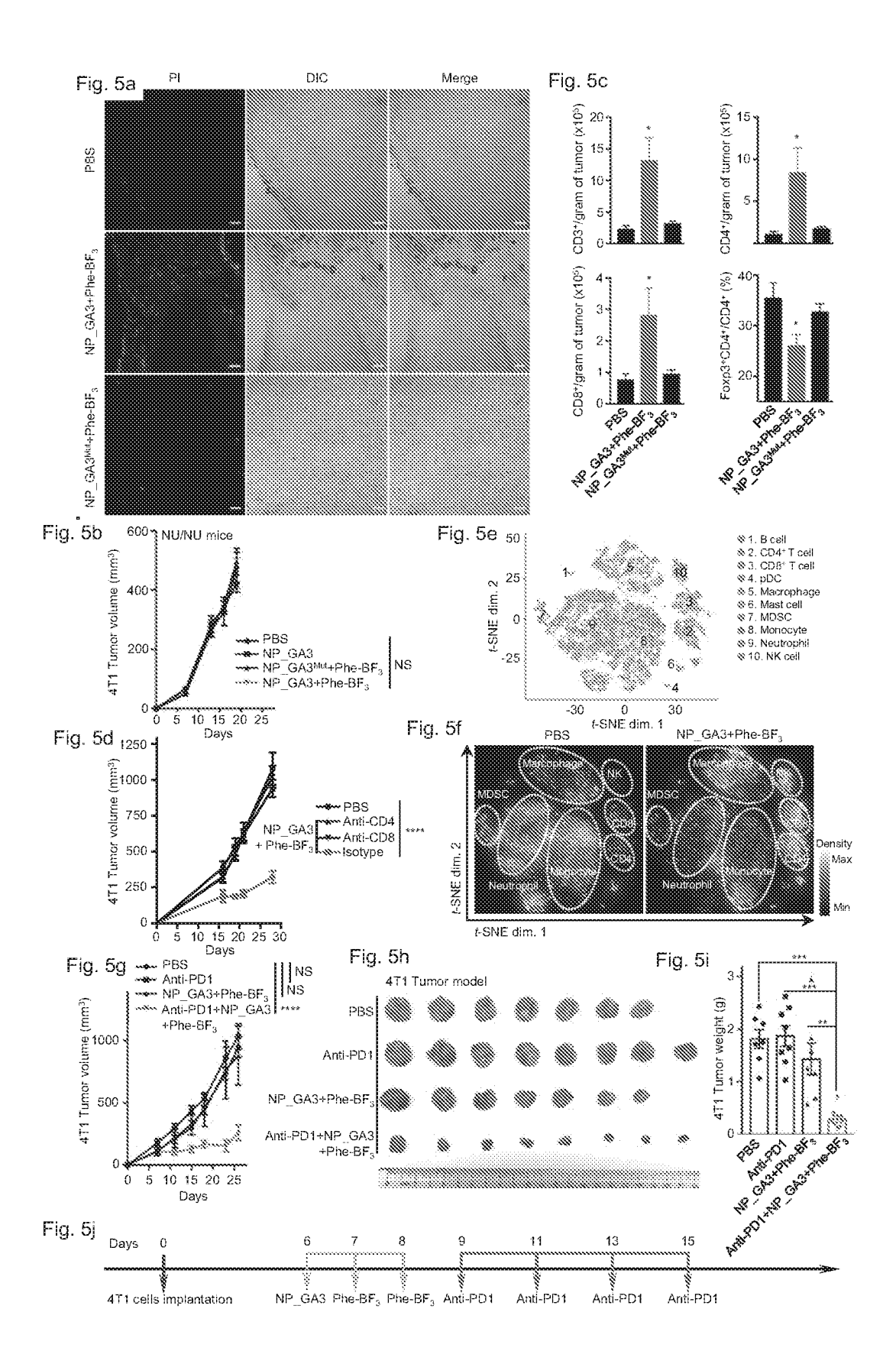
administering to the person an anti-PD1 therapeutic wherein the organotrifluoroborate and the anti-PD1 therapeutic synergistically induce tumor regression in the person; and optionally, detecting a resultant tumor regression in the person.

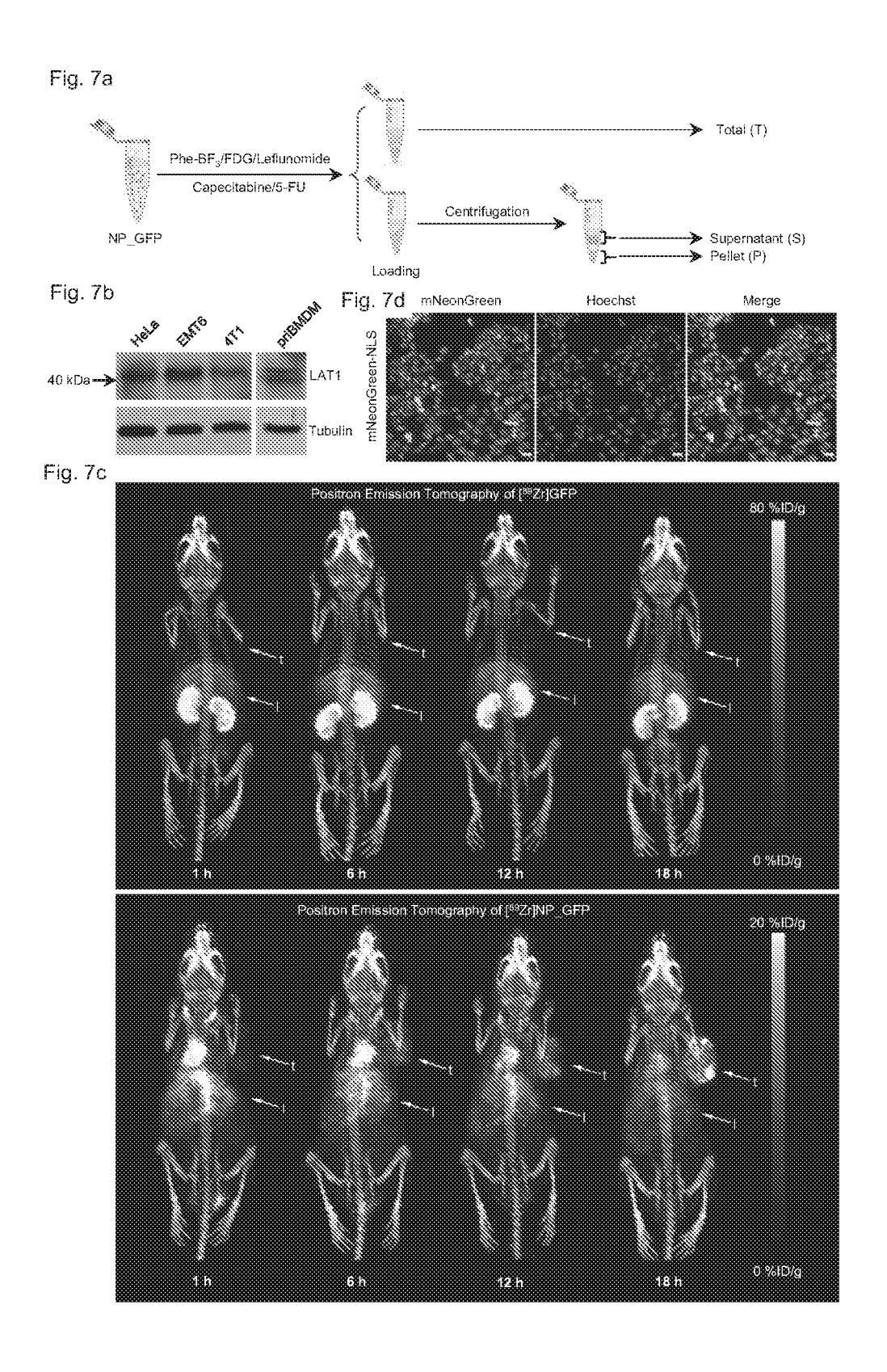


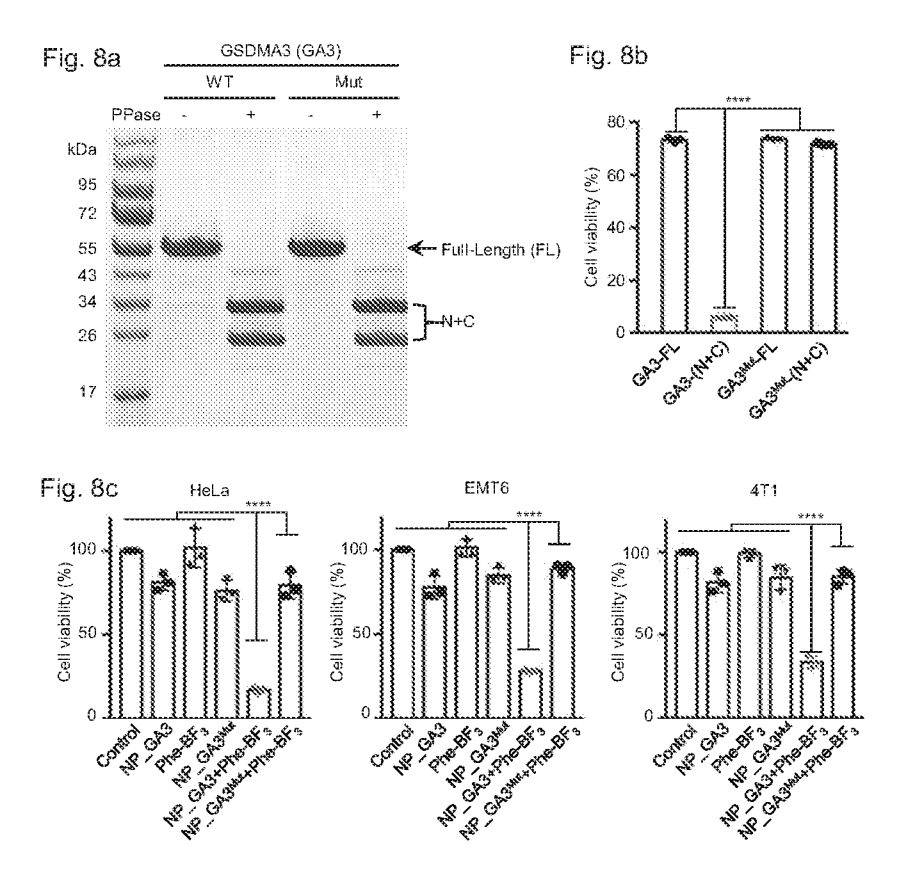


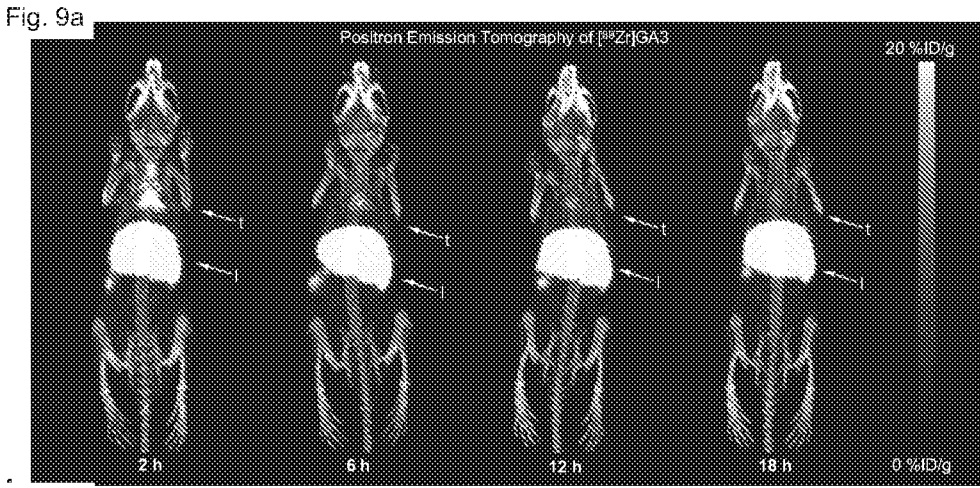






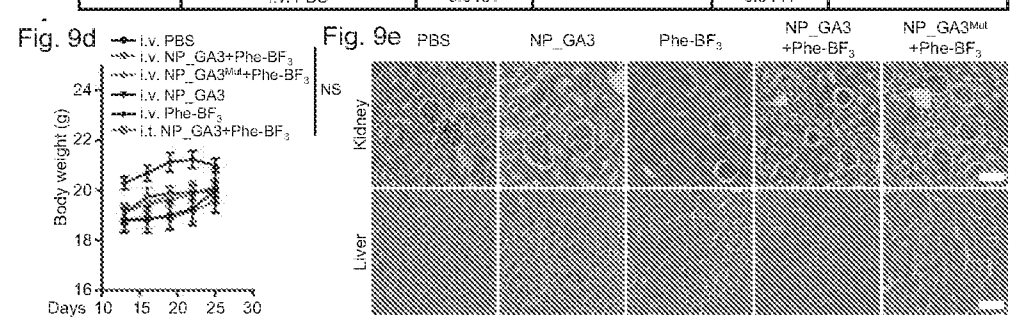


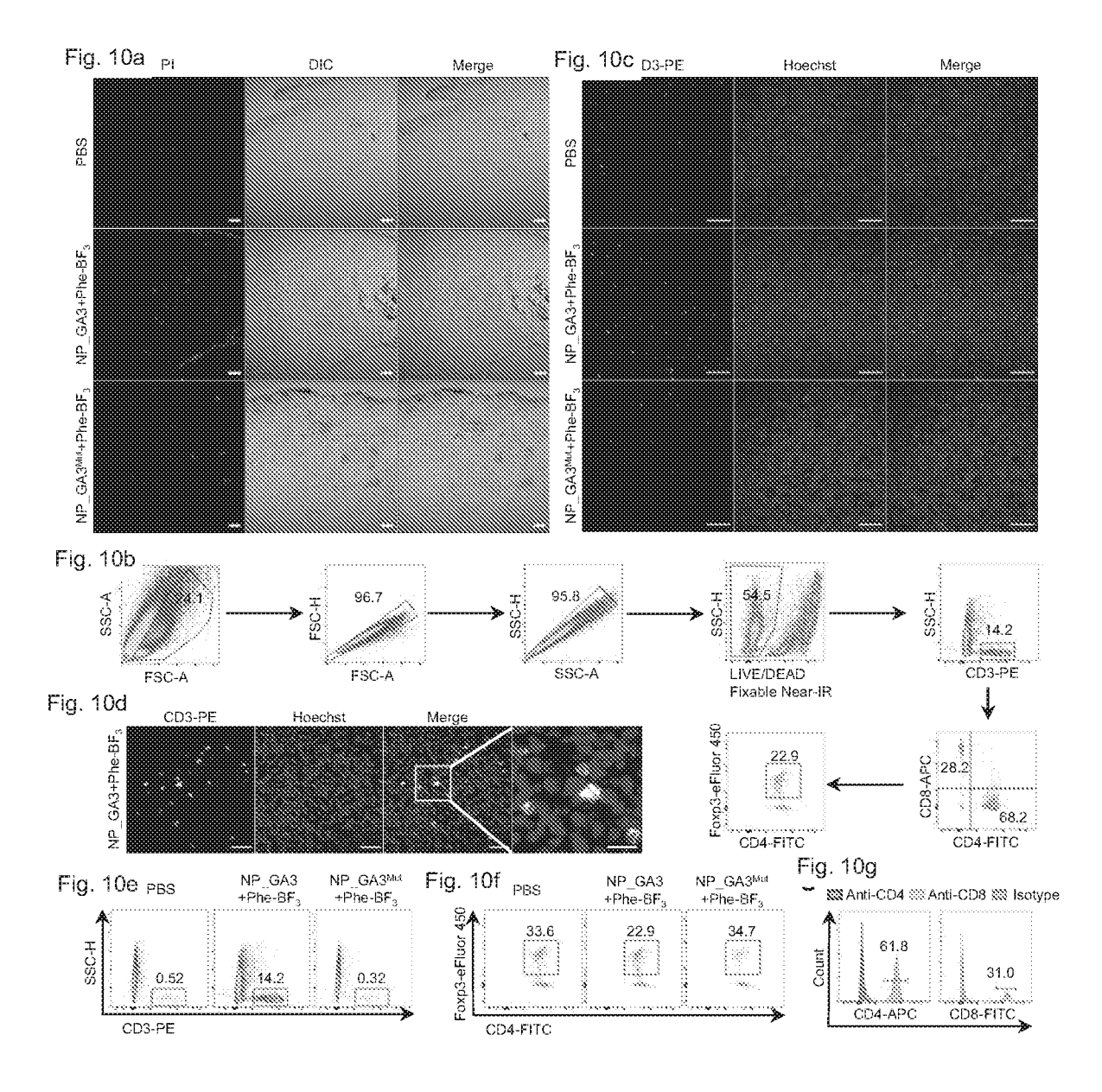


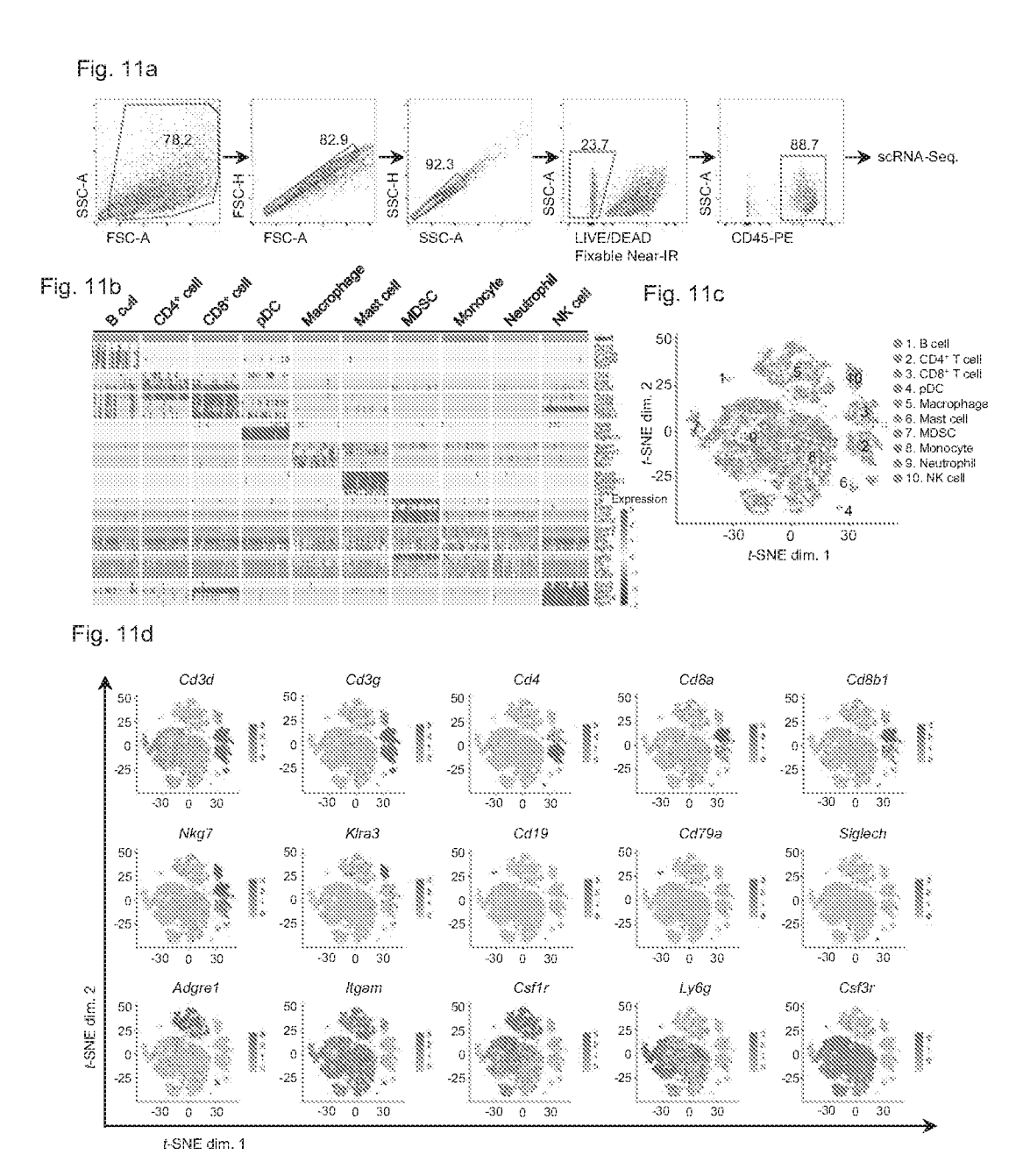


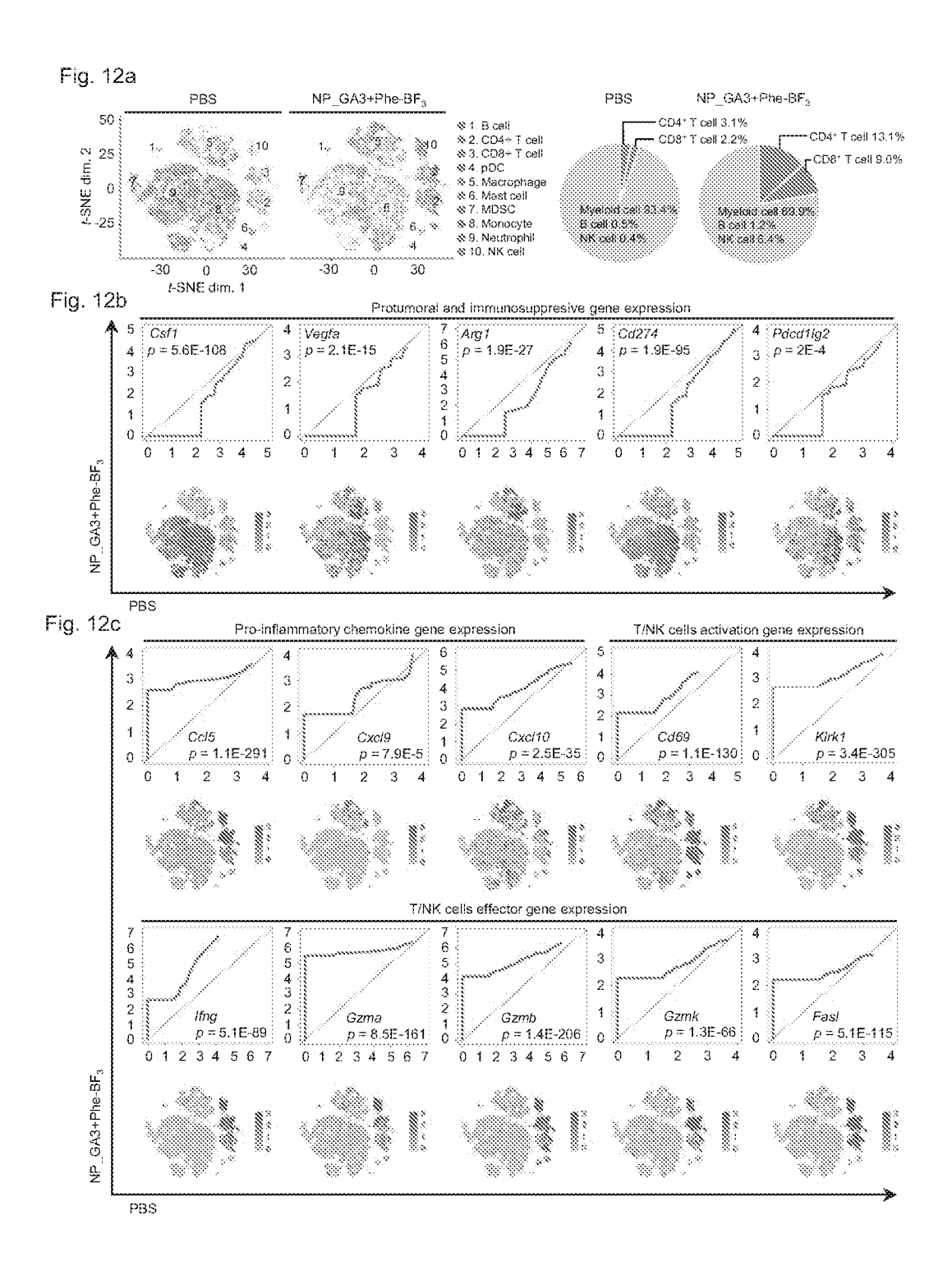


90	0	i.v. NP	_GA3+Phe-BF3	i.t. NP_GA3+Phe-BF3		
Days	Group	P value P value summary		P value	P value summary	
	i.v. NP_GA3 <sup>Mut</sup> +Phe-BF3	0.0003	***	0.0002	***	
D-1100	i.v. NP_GA3	< 0.0001	****	< 0.0001 *****		
Day 22	i.v. Phe-BF3	0.0009	***	0.0005	***	
	i.v. PBS	0.0133	*	0.0107	#	
	i.v. NP_GA3 <sup>Md+</sup> Phe-BF3	< 0.0001	****	< 0.0001	****	
Davide	i.v. NP_GA3	0.0019	**	0.0017	**	
Day 25	i.v. Phe-BF3	0.0002	***	0.0002	***	
}	Ly, PBS	0.0461	*	0.0444	*	









### INTERNATIONAL SEARCH REPORT

International application No.

### PCT/CN2020/108776

### CLASSIFICATION OF SUBJECT MATTER

A61K 45/00(2006.01)i; A61P 35/00(2006.01)i

According to International Patent Classification (IPC) or to both national classification and IPC

#### FIELDS SEARCHED В.

Minimum documentation searched (classification system followed by classification symbols)

A61K; A61P

Documentation searched other than minimum documentation to the extent that such documents are included in the fields searched

Electronic data base consulted during the international search (name of data base and, where practicable, search terms used)

CNABS, CNTXT, DWPI, WOTXT, USTXT, EPTXT, CNKI, Web of Science: SHAO Feng, LIU Zhibo, WANG Qinyang, pyroptosis, tumor,tumour,cancer,gasdermin,bioorthogonal,trifluoroborate,trifluoride,boron,cleave,silyl,ether,desilylation,deprotection

#### C. DOCUMENTS CONSIDERED TO BE RELEVANT

Further documents are listed in the continuation of Box C.

Category*	Citation of document, with indication, where appropriate, of the relevant passages	Relevant to claim No.
X	WO 2018049014 A1 (TRUSTEES OF TUFTS COLLEGE) 15 March 2018 (2018-03-15) claims 1-2	1-2
Y	WO 2018049014 A1 (TRUSTEES OF TUFTS COLLEGE) 15 March 2018 (2018-03-15) claims 1-2	3-10
A	WO 2018106753 A1 (THE GENERAL HOSPITAL CORPORATION) 14 June 2018 (2018-06-14) the abstract	1-20
PX	WANG Qinyang et al. "A bioorthogonal system reveals antitumour immune function of pyroptosis."  Nature., 11 March 2020 (2020-03-11), pages 1-7	1-20
Y	KELLY David R.et al. "The Cleavage of t-Butyldimethylsilyl Ethers with Boron Trifluoride Etherate."  Synthetic Communications., Vol. 9, No. 4, 31 December 1979 (1979-12-31), pages 295-299	6-20

* "A"	Special categories of cited documents: document defining the general state of the art which is not considered to be of particular relevance	"T"	later document published after the international filing date or priority date and not in conflict with the application but cited to understand the principle or theory underlying the invention		
"E"	earlier application or patent but published on or after the international filing date document which may throw doubts on priority claim(s) or which is	"X"	document of particular relevance; the claimed invention cannot be considered novel or cannot be considered to involve an inventive step when the document is taken alone		
"o"	cited to establish the publication date of another citation or other special reason (as specified) document referring to an oral disclosure, use, exhibition or other means	"Y"	document of particular relevance; the claimed invention cannot be considered to involve an inventive step when the document is combined with one or more other such documents, such combination becomes a claimed in the contract of the contr		
"P"	document published prior to the international filing date but later than the priority date claimed	"&"	being obvious to a person skilled in the art document member of the same patent family		
Date of the actual completion of the international search		Date of mailing of the international search report			
03 November 2020		19 November 2020			
Name	e and mailing address of the ISA/CN	Authorized officer			
National Intellectual Property Administration, PRC 6, Xitucheng Rd., Jimen Bridge, Haidian District, Beijing 100088 China			JIN,Wu		
Facsimile No. (86-10)62019451			Telephone No. <b>86-(10)-53961850</b>		

See patent family annex.

## INTERNATIONAL SEARCH REPORT

International application No.

		PCT/CN2020/108776			
	UMENTS CONSIDERED TO BE RELEVANT		<b>D.</b> 1		
Category*	Citation of document, with indication, where appropriate, of the rele		Relevant to claim No.		
Y	Y SHI Jianjin et al. "Pyroptosis: Gasdermin-Mediated Programmed Necrotic Cell Death."  Trends in Biochemical Sciences., Vol. 42, No. 4, 30 April 2017 (2017-04-30), pages 245-254				
Y	LI Jie et al. "Development and Application of Bond Cleavage Reactions in Chemistry."  Nature Chemical Biology., Vol. 12, 16 February 2016 (2016-02-16), pages 129-137	Bioorthogonal	4-20		

## INTERNATIONAL SEARCH REPORT

International application No.

# PCT/CN2020/108776

Box No. II		Observations where certain claims were found unsearchable (Continuation of item 2 of first sheet)						
This international search report has not been established in respect of certain claims under Article 17(2)(a) for the following reasons:								
1.		ns Nos.: 1-20 use they relate to subject matter not required to be searched by this Authority, namely:						
	[1]	Claims 1-10 relate to methods of inducing an antitumor immune response, claims 11-20 relate to a method for releasing in a cell (e.g. cancer cell of a tumor) a client molecule (e.g. cytotoxic drug or tumor suppressor protein) from a silyl ether containing linker. Thus, claims 1-20 direct to methods of treating diseases for human or animal body, and do not meet the criteria set out in PCT Rule 39.1 (iv). The search has been carried out and based on the use of pyroptosis activator in manufacture of medicament for inducing an antitumor immune response, or the use of organotrifluoroborate in manufacture of medicament/reagent for releasing in a cell a client molecule from a silyl ether containing linker.						
2.	becau	ns Nos.: use they relate to parts of the international application that do not comply with the prescribed requirements to such an at that no meaningful international search can be carried out, specifically:						
3.		ns Nos.: use they are dependent claims and are not drafted in accordance with the second and third sentences of Rule 6.4(a).						

# INTERNATIONAL SEARCH REPORT Information on patent family members

International application No.

# PCT/CN2020/108776

	Patent document cited in search report		Publication date (day/month/year)	Patent family member(s)		r(s)	Publication date (day/month/year)
WO	2018049014	A1	15 March 2018	EP	3509604	<b>A</b> 1	17 July 2019
				KR	20190045311	A	02 May 2019
				WO	2018049015	<b>A</b> 1	15 March 2018
				WO	2018049027	<b>A</b> 1	15 March 2018
				WO	2018049008	$\mathbf{A}1$	15 March 2018
				US	2020022956	<b>A</b> 1	23 January 2020
				US	2019209525	$\mathbf{A}1$	11 July 2019
				CA	3036202	<b>A</b> 1	15 March 2018
				CN	109906082	A	18 June 2019
				EP	3509604	A4	26 August 2020
				JP	2019530671	A	24 October 2019
WO	2018106753	<b>A</b> 1	14 June 2018	US	2019336577	<b>A</b> 1	07 November 2019